35. Particle Detectors for Non-Accelerator Physics

Revised 2017. See the various sections for authors.

35.1. Introduction

Non-accelerator experiments have become increasingly important in particle physics. These include classical cosmic ray experiments, neutrino oscillation measurements, and searches for double-beta decay, dark matter candidates, and magnetic monopoles. The experimental methods are sometimes those familiar at accelerators (plastic scintillators, drift chambers, TRD's, *etc.*) but there is also instrumentation either not found at accelerators or applied in a radically different way. Examples are atmospheric scintillation detectors (Fly's Eye), massive Cherenkov detectors (Super-Kamiokande, IceCube), ultracold solid state detectors (CDMS). And, except for the cosmic ray detectors, radiologically ultra-pure materials are required.

In this section, some more important detectors special to terrestrial non-accelerator experiments are discussed. Techniques used in both accelerator and non-accelerator experiments are described in Sec. 28, Particle Detectors at Accelerators, some of which have been modified to accommodate the non-accelerator nuances.

Space-based detectors also use some unique instrumentation, but these are beyond the present scope of RPP.

35.2. High-energy cosmic-ray hadron and gamma-ray detectors

35.2.1. *Atmospheric fluorescence detectors* :

Revised August 2017 by L.R. Wiencke (Colorado School of Mines).

Cosmic-ray fluorescence detectors (FDs) use the atmosphere as a giant calorimeter to measure isotropic scintillation light that traces the development profiles of extensive air showers. An extensive air shower (EAS) is produced by the interactions of ultra high-energy ($E > 10^{17}$ eV) subatomic particles in the stratosphere and upper troposphere. The amount of scintillation light generated by an EAS is proportional to the energy deposited in the atmosphere and nearly independent of the primary species. With energies extending beyond 10^{20} eV these are the highest energy subatomic particles known to exist. In addition to particle arrival directions, energy spectra and primary composition, the astroparticle science investigated with FDs also includes multi-messenger studies, searches for high energy photons, neutrinos, monopoles and deeply penetrating forms of dark matter.

Previous experiments with FDs included the pioneering Fly's Eye [1,2], and the High Resolution Fly's Eye (HiRes and HiRes prototype) [3]. The current generation of experiments include the Telescope Array (TA) [4] in the northern hemisphere, and the much larger Pierre Auger Observatory (Auger) [5] in the southern hemisphere. Both are hybrid observatories. Their FD telescopes overlook sparse arrays of particle detectors on the ground. Select parameters are listed in Table 35.1. TA and Auger have each one FD site populated with additional telescopes that view up to 60° in elevation to measure lower EASs using a combination of scintillation and direct Cherenkov light. The Auger FD also measures UV scintillation that traces the development of atmospheric transient luminous events called ”Elves” that are initiated by lightning [6]. At TA a prototype FD telescope, dubbed FAST [7], has observed EASs using wide field of view PMTs and fast timing.

Observatory	Fly's Eye	HiRes	Telescope Array	Pierre Auger
Location	Dugway UT US	Dugway UT US	Delta UT US	Malargüe AR
Start-End	1981-1992	1996-2006	2008-present	2005-present
Sites (note 1)	2 (1986)	2 (1999)	3 (2008)	4 (2008)
Separation	3.3 km	12.6 km	31-40 km	39-62 km
Telescopes/site	67,18	21,42	12,12,14+10	6, 6, 6, 6+3
Pixel FOV	5.5°	1°	1°	1.5°
Telescope FOV Azi×Elv	≈18°×≈18°	16°×13.5°	18°×15° (note 2)	30°×28.1°
Light collection area (note 3)	$1.95\,\mathrm{m}^2$ - $0.25\,\mathrm{m}^2$	$3.72\,\mathrm{m}^2$ - $0.5\,\mathrm{m}^2$	$6.8\,\mathrm{m}^2$ - $0.85\,\mathrm{m}^2$ (for 2 sites)	$3.80\,\mathrm{m}^2$ - $0.80\,\mathrm{m}^2$ (modified schmidt)
Energy Scale Uncertainty	≤40%	≈20%	≈20%	14%

Table 35.1: Parameters of major fluorescence detectors. Note 1: Year when all FD sites were operational. Note 2: At TA 1 of the 3 FD sites features 24 telescopes from the HiRes experiment. Note 3: A-C for one telescope where A is the full area and C the area obscured by the camera and support structures. Thus A-C is the effective light collecting area. For the modified Schmidt design at Auger, the area of the entrance pupil, A, is listed because the pupil is smaller than the mirror and thus defines the entrance aperture. For the other experiments, the area of the mirror, A, is listed.

The fluorescence light is emitted primarily between 290 and 430 nm (Fig. 35.1) with major lines at 337, 357, and 391 nm, when relativistic charged particles, primarily electrons and positrons, excite nitrogen molecules in air, resulting in transitions of the 1P and 2P systems. Reviews and references for the pioneering and recent laboratory measurements of fluorescence yield, $Y(\lambda, P, T, u)$, including dependence on wavelength (λ), temperature (T), pressure (p), and humidity (u) may be found in Refs. 8–10. The results of various laboratory experiments have been combined (Fig. 35.2) to obtain an absolute average and uncertainty for Y(337 nm, 800 hPa, 293 K, dry air) of 7.04 ± 0.24 ph/MeV after corrections for different electron beam energies and other factors. The units of ph/MeV correspond to the number of fluorescence photons produced per MeV of energy deposited in the atmosphere by the electromagnetic component of an EAS.

An FD element (telescope) consists of a non-tracking spherical mirror of less than astronomical quality, a close-packed “camera” of photomultiplier tubes (PMTs) near the focal plane, and a flash ADC readout system with a pulse and track-finding trigger scheme [11]. The major experiments listed in Table 35.1 all use conventional

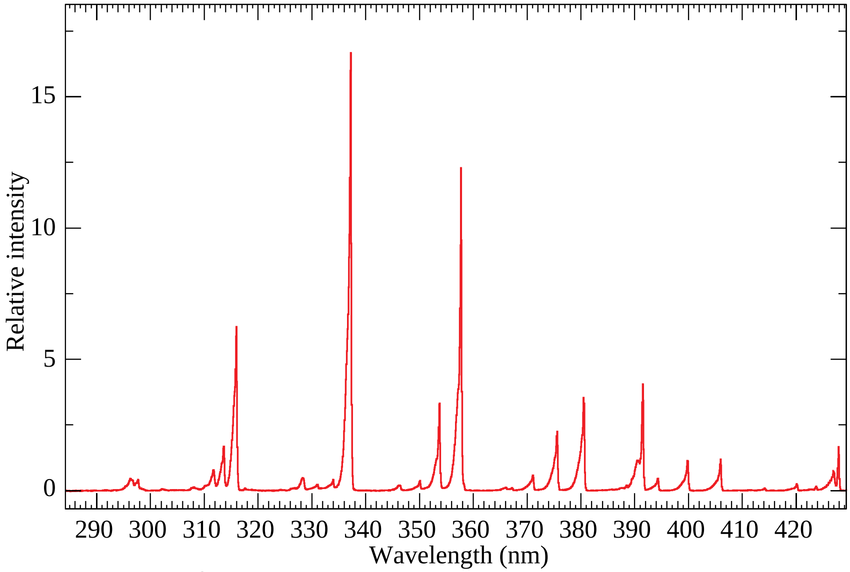

Figure 35.1: Measured fluorescence spectrum excited by 3 MeV electrons in dry air at 800 hPa and 293 K. Airfly experiment. Figure from Ref [12].

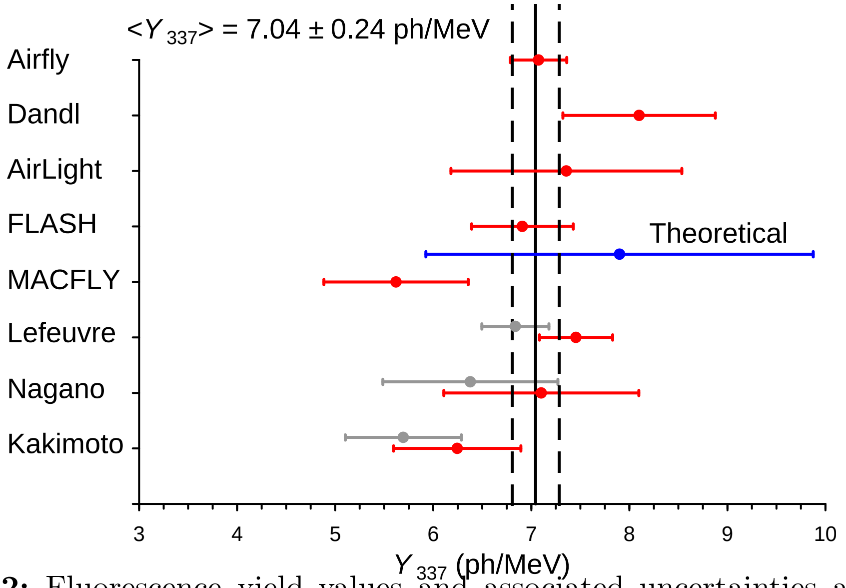

Figure 35.2: Fluorescence yield values and associated uncertainties at 337 nm (Y_{337}) in dry air at 800 hPa and 293 K The methodology and corrections that were applied to obtain the average and the uncertainty are discussed extensively in this reference. The vertical axis denotes different laboratory experiments that measured FY. The gray bars show three of the original measurements to illustrate the scale of the corrections applied. Figure from Ref [13].

PMTs (for example, Hamamatsu R9508 or Photonis XP3062) with grounded cathodes and AC coupled readout. Segmented mirrors have been fabricated from slumped or slumped/polished glass with an anodized aluminum coating or fabricated using shaped aluminum that was then chemically anodized with $AlMgSiO_5$. A broadband UV filter (custom fabricated or Schott MUG-6) reduces background light such as starlight, airglow, man-made light pollution, and airplane strobe-lights.

At 10^{20} eV, where the flux drops below 1 EAS/km^{2}century, the aperture for an eye of adjacent FD telescopes that span the horizon can reach 10^4 km^2 sr. FD operation requires (nearly) moonless nights and clear atmospheric conditions, which imposes a duty cycle of about 10%. Arrangements of LEDs, calibrated diffuse sources [14], pulsed UV lasers [15], LIDARs* and IR detectors that are sensitive to clouds are used for photometric calibration, atmospheric calibration [16], and determination of exposure [17]. For purposes of optical transmission, the atmosphere is treated as a dominant molecular component and a secondary aerosol component. The latter is well described [18] by molecular scattering theory and models derived from radiosonde measurements. The aerosol component can include dust, haze and pollution and the aerosol optical depth profile must be measured on site in the UV during FD data taking.

The EAS generates a track consistent with a light source moving at $v = c$ across the FOV. The number of photons (N_γ) as a function of atmospheric depth (X) can be expressed as [9]

$$\frac{\mathrm{d}N_\gamma}{\mathrm{d}X} = \frac{dE_{\mathrm{dep}}^{\mathrm{tot}}}{dX} \int Y(\lambda, P, T, u) \cdot \tau_{\mathrm{atm}}(\lambda, X) \cdot \varepsilon_{\mathrm{FD}}(\lambda)\mathrm{d}\lambda, \tag{35.1}$$

where $\tau_{atm}(\lambda, X)$ is the atmospheric transmission, including wavelength (λ) dependence, and $\varepsilon_{\mathrm{FD}}(\lambda)$ is the FD efficiency. $\varepsilon_{\mathrm{FD}}(\lambda)$ includes geometric factors and collection efficiency of the optics, quantum efficiency of the PMTs, and other throughput factors. The typical systematic uncertainties, τ_{atm} (10%) and $\varepsilon_{\mathrm{FD}}$ (photometric calibration 10%), currently dominate the systematic uncertainty the absolute EAS energy scale. FD energy resolution, defined as event-to-event statistical uncertainty, is typically less than 10% for final data samples used for science analysis.

Analysis methods to reconstruct the EAS profile and deconvolve the contributions of re-scattered scintillation light, and direct and scattered Cherenkov light are described in [1] and more recently in [19]. The EAS energy is typically obtained by integrating over the Gaisser-Hillas function [20]

$$E_{\mathrm{cal}} = \int_0^\infty [w_{\mathrm{max}} \left(\frac{X - X_0}{X_{\mathrm{max}} - X_0}\right)^{(X_{\mathrm{max}}-X_0)/\lambda} e^{(X_{\mathrm{max}}-X)/\lambda}]\mathrm{d}X, \tag{35.2}$$

where E_{cal} is the energy of electromagnetic energy component of the EAS and X_{max} is the atmospheric slant depth at which the shower reaches its maximum energy deposit rate. This maximum dE/dX is denoted as w_{max}. X_0 and λ are two shape parameters. The energy of the primary cosmic ray is obtained by correcting E_{cal} upward by about 10% to account for the invisible energy carried by particles that do not interact in the atmosphere. Energy resolution, $\Delta E/E$, of 15-20% is achievable, provided the geometric

---

* "LIDAR stands for "Light Detection and Ranging" and refers here to systems that measure atmospheric properties from the light scattered backwards from laser pulses directed into the sky.

fit of the EAS axis is constrained, typically by multi-eye stereo projection or hybrid observations, and the profile fit of EAS development along the track is constrained by the observed rise and fall about X_{max}. An example of a recorded EAS light profile and its corresponding dE/dX development profile are shown in Fig. 35.3.

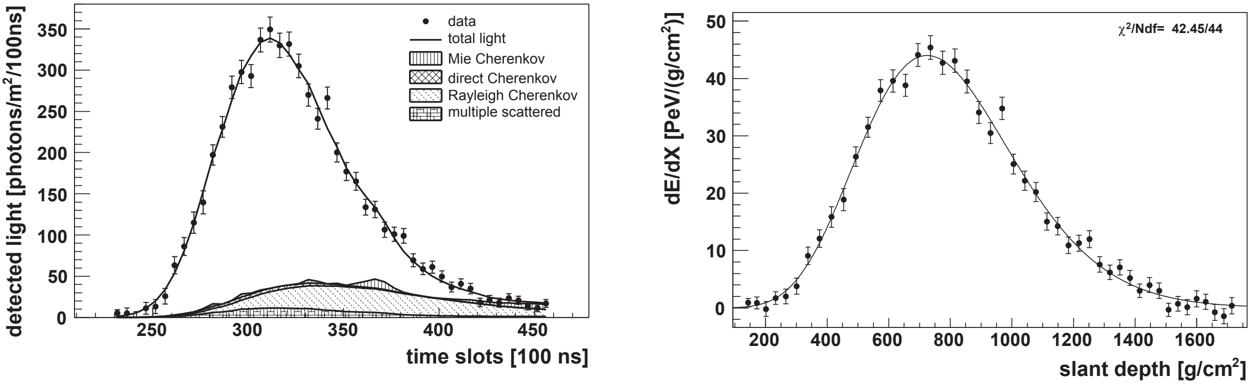

Figure 35.3: Example light profile (left) of one EAS recorded by the Pierre Auger FD and the corresponding profile (right) of energy deposited in the atmosphere vs atmospheric slant depth. The light profiles include the estimated components of Cherenkov light that have been scattered out of the forward beam by the molecular and aerosol (Mie) components of the atmosphere. The reconstructed energy of this EAS was $3.0 \pm 0.2 \times 10^{19}$ eV. Figure from Ref [21].

R&D toward an FD in space is at the design and prototype phase. A proposed space based FD instrument [22] by the JEM-EUSO collaboration would look down on the earth's atmosphere from space to view a much larger area than ground based instruments. Prototypes that have been built and flown include the TUS instrument [23] launched in 2016 onboard the Lomonosov satellite and two FD telescopes flown on stratospheric balloons in 2014 [24] and 2017 [25]. The proposed POEMMA space mission [26] would record scintillation and Cherenkov light from EASs the atmosphere to measure UHECRs and PeV scale cosmogenic tau neutrinos.

35.2.2. *Atmospheric Cherenkov telescopes for high-energy γ-ray astronomy* :

Revised July 2017 by J. Holder (Dept. of Physics and Astronomy & Bartol Research Inst., Univ. of Delaware).

A wide variety of astrophysical objects are now known to produce high-energy γ-ray photons. Leptonic or hadronic particles, accelerated to relativistic energies in the source, produce γ-rays typically through inverse Compton boosting of ambient photons or through the decay of neutral pions produced in hadronic interactions. At energies below $\sim$30 GeV, γ-ray emission can be efficiently detected using satellite or balloon-borne instrumentation, with an effective area approximately equal to the size of the detector (typically < 1 m^2). At higher energies, a technique with much larger effective collection area is desirable to measure astrophysical γ-ray fluxes, which decrease rapidly with increasing energy. Atmospheric Cherenkov detectors achieve effective collection areas of $>10^5$ m^2 by employing the Earth's atmosphere as an intrinsic part of the detection technique.

As described in Chapter 29, a hadronic cosmic ray or high energy γ-ray incident on the Earth's atmosphere triggers a particle cascade, or air shower. Relativistic charged particles in the cascade generate Cherenkov radiation, which is emitted along the shower direction, resulting in a light pool on the ground with a radius of $\sim$130 m. Cherenkov light is produced throughout the cascade development, with the maximum emission occurring when the number of particles in the cascade is largest, at an altitude of $\sim$10 km for primary energies of 100 GeV–1 TeV. Following absorption and scattering in the atmosphere, the Cherenkov light at ground level peaks at a wavelength, $\lambda \approx 300$–350 nm. The photon density is typically $\sim$100 photons/m^2 for a 1 TeV primary, arriving in a brief flash of a few nanoseconds duration. This Cherenkov pulse can be detected from any point within the light pool radius by using large reflecting surfaces to focus the Cherenkov light on to fast photon detectors (Fig. 35.4).

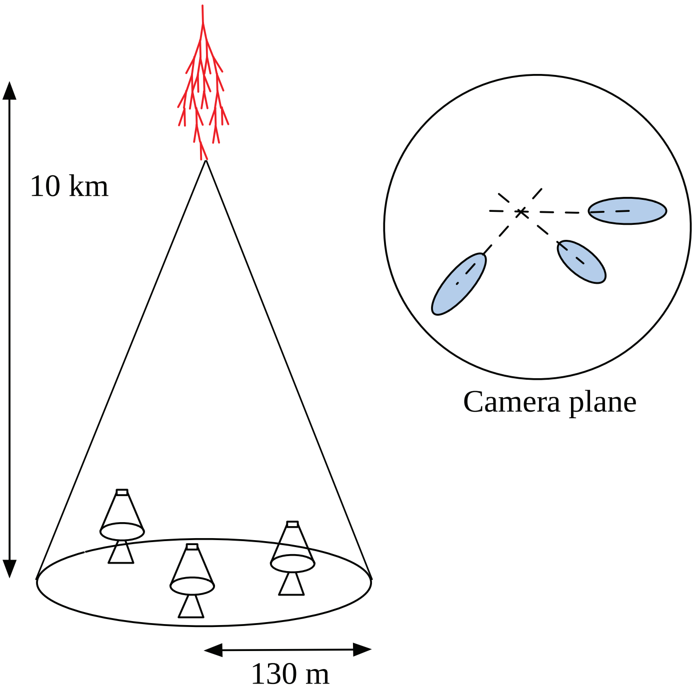

Figure 35.4: A schematic illustration of an imaging atmospheric Cherenkov telescope array. The primary particle initiates an air shower, resulting in a cone of Cherenkov radiation. Telescopes within the Cherenkov light pool record elliptical images; the intersection of the long axes of these images indicates the arrival direction of the primary, and hence the location of a γ-ray source in the sky.

Modern atmospheric Cherenkov telescopes, such as those built and operated by the VERITAS [27], H.E.S.S. [28] and MAGIC [29] collaborations, consist of large ($> 100\,\mathrm{m}^2$) segmented mirrors on steerable altitude-azimuth mounts. A camera made from an array of photosensors is placed at the focus of each mirror and used to record a Cherenkov image of each air shower. In these imaging atmospheric Cherenkov telescopes, single-anode photomultipliers tubes (PMTs) have traditionally been used (2048, in the case of H.E.S.S. II), but multi-anode PMTs and silicon devices now feature in more modern designs.

The telescope cameras typically cover a field-of-view of $3 - 10^\circ$ in diameter. Images are recorded at kHz rates, the vast majority of which are due to showers with hadronic cosmic-ray primaries. The shape and orientation of the Cherenkov images are used to discriminate γ-ray photon events from this cosmic-ray background, and to reconstruct the photon energy and arrival direction. γ-ray images result from purely electromagnetic cascades and appear as narrow, elongated ellipses in the camera plane. The long axis of the ellipse corresponds to the vertical extension of the air shower, and points back towards the source position in the field-of-view. If multiple telescopes are used to view the same shower ("stereoscopy"), the source position is simply the intersection point of the various image axes. Cosmic-ray primaries produce secondaries with large transverse momenta, which initiate sub-showers. Their images are consequently wider and less regular than those with γ-ray primaries and, since the original charged particle has been deflected by Galactic magnetic fields before reaching the Earth, the images have no preferred orientation.

The measurable differences in Cherenkov image orientation and morphology provide the background discrimination which makes ground-based γ-ray astronomy possible. For point-like sources, such as distant active galactic nuclei, modern instruments can reject over 99.999% of the triggered cosmic-ray events, while retaining up to 50% of the γ-ray population. In the case of spatially extended sources, such as Galactic supernova remnants, the background rejection is less efficient, but the technique can be used to produce γ-ray maps of the emission from the source. The angular resolution depends upon the number of telescopes which view the image and the energy of the primary γ-ray, but is typically less than 0.1° per event (68% containment radius) at energies above a few hundred GeV.

The total Cherenkov yield from the air shower is proportional to the energy of the primary particle. The image intensity, combined with the reconstructed distance of the shower core from each telescope, can therefore be used to estimate the primary energy. The energy resolution of this technique, also energy-dependent, is typically 15–20% at energies above a few hundred GeV. Energy spectra of γ-ray sources can be measured over a wide range, depending upon the instrument characteristics, source properties (flux, spectral slope, elevation angle, *etc.*), and exposure time. The effective energy range is typically from 30 GeV to 100 TeV and peak sensitivity lies in the range from 100 GeV to a few TeV.

The first astrophysical source to be convincingly detected using the imaging atmospheric Cherenkov technique was the Crab Nebula [30], with an integral flux of 2.1×10^{-11} photons $\text{cm}^{-2}\ \text{s}^{-1}$ above 1 TeV [31]. Modern imaging atmospheric Cherenkov telescopes have sensitivity sufficient to detect sources with less than 1% of the Crab Nebula flux in a few tens of hours. The TeV source catalog now consists of approximately 200 sources (see e.g. Ref. 32). A large fraction of these were detected by scanning the Galactic plane from the southern hemisphere with the H.E.S.S. telescope array [33]. Recent reviews of the field include [34] and [35], and a historical overview can be found in [36].

Major upgrades of the existing telescope arrays have recently been completed, including the addition of a 28 m diameter central telescope to H.E.S.S. (H.E.S.S. II). Development is also underway for the next generation instrument, the Cherenkov Telescope Array (CTA), which will consist of a northern and a southern hemisphere observatory, with a combined total of more than 100 telescopes [37]. Telescopes of three different sizes are planned, spread over an area of > 1 km^2, providing wider energy coverage, improved angular and energy resolutions, and an order of magnitude improvement in sensitivity relative to existing imaging atmospheric Cherenkov telescopes. Baseline telescope designs are similar to existing devices, but exploit technological developments such as dual mirror optics and silicon photo-detectors.

35.3. Large neutrino detectors

35.3.1. *Deep liquid detectors for rare processes* :

Revised August 2017 by K. Scholberg & C.W. Walter (Duke University)

Deep, large detectors for rare processes tend to be multi-purpose with physics reach that includes not only solar, reactor, supernova and atmospheric neutrinos, but also searches for baryon number violation, searches for exotic particles such as magnetic monopoles, and neutrino and cosmic-ray astrophysics in different energy regimes. The detectors may also serve as targets for long-baseline neutrino beams for neutrino oscillation physics studies. In general, detector design considerations can be divided into high-and low-energy regimes, for which background and event reconstruction issues differ. The high-energy regime, from about 100 MeV to a few hundred GeV, is relevant for proton decay searches, atmospheric neutrinos and high-energy astrophysical neutrinos. The low-energy regime (a few tens of MeV or less) is relevant for supernova, solar, reactor and geological neutrinos.

Large water Cherenkov and scintillator detectors (see Table 35.2) usually consist of a volume of transparent liquid viewed by photomultiplier tubes (PMTs) (see Sec. 34.2); the liquid serves as active target. PMT hit charges and times are recorded and digitized, and triggering is usually based on coincidence of PMT hits within a time window comparable to the detector's light-crossing time. Because photosensors lining an inner surface represent a driving cost that scales as surface area, very large volumes can be used for comparatively reasonable cost. Some detectors are segmented into subvolumes individually viewed by PMTs, and may include other detector elements (*e.g.*, tracking detectors). Devices to increase light collection, *e.g.*, reflectors or waveshifter plates, may be employed. A common configuration is to have at least one concentric outer layer of liquid material separated from the inner part of the detector to serve as shielding against ambient background. If optically separated and instrumented with PMTs, an outer layer may also serve as an active veto against entering cosmic rays and other background events. The PMTs for large detectors typically range in size from 20 cm to 51 cm diameter, and typical quantum efficiencies are in the 20–25% range for scintillation and water-Cherenkov photons. PMTs with higher quantum efficiencies, 35% or higher, have recently become available. The active liquid volume requires purification and there may be continuous recirculation of liquid. For large homogeneous detectors, the event interaction vertex is determined using relative timing of PMT hits, and energy deposition is determined from the number of recorded photoelectrons. A "fiducial volume" is usually defined within the full detector volume, some distance away from the PMT array. Inside the fiducial volume,

Table 35.2: Properties of large detectors for rare processes. If total target mass is divided into large submodules, the number of subdetectors is indicated in parentheses. Projects with first data expected in 2020 or later are indicated in italics.

Detector	Mass, kton (modules)	PMTs (diameter, cm)	ξ	p.e./MeV	Dates
Baksan	0.33, scint (3150)	1/module (15)	segmented	40	1980–
MACRO	0.56, scint (476)	2-4/module (20)	segmented	18	1989–2000
LVD	1, scint. (840)	3/module (15)	segmented	15	1992–
KamLAND	0.41[f], scint	1325(43)+554(51)*	34%	460	2002–
Borexino	0.1[f], scint	2212 (20)	30%	500	2007–
SNO+	0.78, scint	9438 (20)	54%	400–900	2017 (exp.)
CHOOZ	0.005, scint (Gd)	192 (20)	15%	130	1997–1998
Double Chooz	0.017, scint (Gd)(2)	534/module (20)	13%	180	2011–
Daya Bay	0.160, scint (Gd)(8)	192/module (20)	5.6%[†]	100	2011–
RENO	0.032, scint (Gd)(2)	342/module (25)	12.6%	100	2011–
JUNO	20.0[f], scint	17000 (51)/25000 (8)	75%	1200	2020 (exp.)
IMB-1	3.3[f], H_2O	2048 (12.5)	1%	0.25	1982–1985
IMB-2	3.3[f], H_2O	2048 (20)	4.5%	1.1	1987–1990
Kam I	0.88/0.78[f], H_2O	1000/948 (51)	20%	3.4	1983–1985
Kam II	1.04[f], H_2O	948 (51)	20%	3.4	1986–1990
Kam III	1.04[f], H_2O	948 (51)	20%[‡]	4.3	1990–1995
SK I	22.5[f], H_2O	11146 (51)	40%	6	1996–2001
SK II	22.5[f], H_2O	5182 (51)	19%	3	2002–2005
SK III-IV	22.5[f], H_2O	11129 (51)	40%	6	2006–
SK-Gd	22.5[f], H_2O (Gd)	11129 (51)	40%	6	2019 (exp.)
Hyper-K	187[f], H_2O**	40000 (51)	40%	12	2026 (exp.)
SNO	1, D_2O/1.7, H_2O	9438 (20)	31% [§]	9	1999–2006

[f] indicates typical fiducial mass used for data analysis; this may vary by physics topic.

* Measurements made before 2003 only considered data from the 43 cm PMTs.

[†] The effective Daya Bay coverage is 12% with top and bottom reflectors.

[‡] The effective Kamiokande III coverage was 25% with light collectors.

** A second staged module is planned.

[§] The effective SNO coverage was 54% with light collectors.

enough PMTs are illuminated per event that reconstruction is considered reliable, and furthermore, entering background from the enclosing walls is suppressed by a buffer of self-shielding. PMT and detector optical parameters are calibrated using laser, LED, or other light sources. Quality of event reconstruction typically depends on photoelectron yield, pixelization and timing.

Because in most cases one is searching for rare events, large detectors are usually sited underground to reduce cosmic-ray-related background (see Chapter 29). The minimum depth required varies according to the physics goals [38].

35.3.1.1. *Liquid scintillator detectors:*

Past and current large underground detectors based on hydrocarbon scintillators include LVD, MACRO, Baksan, Borexino, KamLAND and SNO+; JUNO is a future detector. Experiments at nuclear reactors include CHOOZ, Double CHOOZ, Daya Bay, and RENO. Organic liquid scintillators (see Sec. 34.3.0) for large detectors are chosen for high light yield and attenuation length, good stability, compatibility with other detector materials, high flash point, low toxicity, appropriate density for mechanical stability, and low cost. They may be doped with waveshifters and stabilizing agents. Popular choices are pseudocumene (1,2,4-trimethylbenzene) with a few g/L of the PPO (2,5-diphenyloxazole) fluor, and linear alkylbenzene (LAB). In a typical detector configuration there will be active or passive regions of undoped scintillator, non-scintillating mineral oil or water surrounding the inner neutrino target volume. A thin vessel or balloon made of nylon, acrylic or other material transparent to scintillation light may contain the inner target; if the scintillator is buoyant with respect to its buffer, ropes may hold the balloon in place. For phototube surface coverages in the 20–40% range, yields in the few hundreds of photoelectrons per MeV of energy deposition can be obtained. Typical energy resolution is about $7\%/\sqrt{E(\mathrm{MeV})}$, and typical position reconstruction resolution is a few tens of cm at ~ 1 MeV, scaling as $\sim N^{-1/2}$, where N is the number of photoelectrons detected.

Shallow detectors for reactor neutrino oscillation experiments require excellent muon veto capabilities. For $\bar{\nu}_e$ detection via inverse beta decay on free protons, $\bar{\nu}_e + p \rightarrow n + e^+$, the neutron is captured by a proton on a ~180 μs timescale, resulting in a 2.2 MeV γ ray, observable by Compton scattering and which can be used as a tag in coincidence with the positron signal. The positron annihilation γ rays may also contribute. Inverse beta decay tagging may be improved by addition of Gd at ~0.1% by mass, which for natural isotope abundance has a ~49,000 barn cross-section for neutron capture (in contrast to the 0.3 barn cross-section for capture on free protons). Gd capture takes ~30 μs, and is followed by a cascade of γ rays adding up to about 8 MeV. Gadolinium doping of scintillator requires specialized formulation to ensure adequate attenuation length and stability.

Scintillation detectors have an advantage over water Cherenkov detectors in the lack of Cherenkov threshold and the high light yield. However, scintillation light emission is nearly isotropic, and therefore directional capabilities are relatively weak. Liquid scintillator is especially suitable for detection of low-energy events. Radioactive backgrounds are a serious issue, and include long-lived cosmogenics. To go below a few MeV, very careful selection of materials and purification of the scintillator is required (see Sec. 35.6). Fiducialization and tagging can reduce background. One can also dissolve neutrinoless double beta decay ($0\nu\beta\beta$) isotopes in scintillator. This has been realized by

KamLAND-Zen, which deployed a 1.5 m-radius balloon containing enriched Xe dissolved in scintillator inside KamLAND, and ^{130}Te is planned for SNO+. Although for this approach, energy resolution is poor compared to other $0\nu\beta\beta$ search experiments, the quantity of isotope can be so large that the kinematic signature of $0\nu\beta\beta$ would be visible as a clear feature in the spectrum.

35.3.1.2. *Water Cherenkov detectors:*

Very large imaging water detectors reconstruct ten-meter-scale Cherenkov rings produced by charged particles (see Sec. 34.5.0). The first such large detectors were IMB and Kamiokande. The only currently existing instance of this class of detector, with fiducial mass of 22.5 kton and total mass of 50 kton, is Super-Kamiokande (Super-K, SK). Hyper-Kamiokande (Hyper-K) plans at least one, and possibly two, detectors with 187-kton fiducial mass. For volumes of this scale, absorption and scattering of Cherenkov light are non-negligible, and a wavelength-dependent factor $\exp(-d/L(\lambda))$ (where d is the distance from emission to the sensor and $L(\lambda)$ is the attenuation length of the medium) must be included in the integral of Eq. (34.5) for the photoelectron yield. Attenuation lengths on the order of 100 meters have been achieved.

Cherenkov detectors are excellent electromagnetic calorimeters, and the number of Cherenkov photons produced by an e/γ is nearly proportional to its kinetic energy. For massive particles, the number of photons produced is also related to the energy, but not linearly. For any type of particle, the *visible energy* $E_{\rm vis}$ is defined as the energy of an electron which would produce the same number of Cherenkov photons. The number of collected photoelectrons depends on the scattering and attenuation in the water along with the photo-cathode coverage, quantum efficiency and the optical parameters of any external light collection systems or protective material surrounding them. Event-by-event corrections are made for geometry and attenuation. For a typical case, in water $N_{\rm p.e.} \sim 15\,\xi\,E_{\rm vis}({\rm MeV})$, where ξ is the effective fractional photosensor coverage. Cherenkov photoelectron yield per MeV of energy is relatively small compared to that for scintillator, *e.g.*, $\sim$ 6 pe/MeV for Super-K with a PMT surface coverage of $\sim 40\%$. In spite of light yield and Cherenkov threshold issues, the intrinsic directionality of Cherenkov light allows individual particle tracks to be reconstructed. Vertex and direction fits are performed using PMT hit charges and times, requiring that the hit pattern be consistent with a Cherenkov ring.

High-energy ($\sim$100 MeV or more) neutrinos from the atmosphere or beams interact with nucleons; for the nucleons bound inside the ^{16}O nucleus, nuclear effects must be considered both at the interaction and as the particles leave the nucleus. Various event topologies can be distinguished by their timing and fit patterns, and by presence or absence of light in a veto. "Fully-contained" events are those for which the neutrino interaction final state particles do not leave the inner part of the detector; these have their energies relatively well measured. Neutrino interactions for which the lepton is not contained in the inner detector sample have higher-energy parent neutrino energy distributions. For example, in "partially-contained" events, the neutrino interacts inside the inner part of the detector but the lepton (almost always a muon, since only muons are penetrating) exits. "Upward-going muons" can arise from neutrinos which interact in the rock below the detector and create muons which enter the detector and either stop, or go all the way through (entering downward-going muons cannot be distinguished from cosmic rays). At high energies, multi-photoelectron hits are likely and the charge collected by each PMT (rather than the number of PMTs firing) must be used; this degrades the energy resolution to approximately $2\%/\sqrt{\xi\, E_{\rm vis}({\rm GeV})}$. The absolute energy scale in this regime can be known to ∼2–3% using cosmic-ray muon energy deposition, Michel electrons and π^0 from atmospheric neutrino interactions. Typical vertex resolutions for GeV energies are a few tens of cm [39]. Angular resolution for determination of the direction of a charged particle track is a few degrees. For a neutrino interaction, because some final-state particles are usually below Cherenkov threshold, knowledge of direction of the incoming neutrino direction itself is generally worse than that of the lepton direction, and dependent on neutrino energy.

Multiple particles in an interaction (so long as they are above Cherenkov threshold) may be reconstructed, allowing for the exclusive reconstruction of final states. In searches for proton decay, multiple particles can be kinematically reconstructed to form a decaying nucleon. High-quality particle identification is also possible: γ rays and electrons shower, and electrons scatter, which results in fuzzy rings, whereas muons, pions and protons make sharp rings. These patterns can be quantitatively separated with high reliability using maximum likelihood methods [40]. A e/μ misidentification probability of $\sim 0.4\%/\xi$ in the sub-GeV range is consistent with the performance of several experiments for $4\% < \xi < 40\%$. Sources of background for high energy interactions include misidentified cosmic muons and anomalous light patterns when the PMTs sometimes "flash" and emit photons themselves. The latter class of events can be removed using its distinctive PMT signal patterns, which may be repeated. More information about high energy event selection and reconstruction may be found in reference [41].

In spite of the fairly low light yield, large water Cherenkov detectors may be employed for reconstructing low-energy events, down to *e.g.* ∼ 4-5 MeV for Super-K [42]. Low-energy neutrino interactions of solar neutrinos in water are predominantly elastic scattering off atomic electrons; single electron events are then reconstructed. At solar neutrino energies, the visible energy resolution ($\sim 30\%/\sqrt{\xi\, E_{\rm vis}({\rm MeV})}$) is about 20% worse than photoelectron counting statistics would imply. Using an electron LINAC and/or nuclear sources, approximately 0.5% determination of the absolute energy scale has been achieved at solar neutrino energies. Angular resolution is limited by multiple scattering in this energy regime (25–30°). At these energies, radioactive backgrounds become a dominant issue. These backgrounds include radon in the water itself or emanated from detector materials, and γ rays from the rock and detector materials. In the few to few tens of MeV range, radioactive products of cosmic-ray-muon-induced spallation are troublesome, and are removed by proximity in time and space to preceding muons, at some cost in dead time. Gadolinium doping using 0.2% $\mathrm{Gd_2(SO_4)_3}$ is planned for Super-K to improve selection of low-energy $\bar{\nu}_e$ and other events with accompanying neutrons [43].

The Sudbury Neutrino Observatory (SNO) detector [44] is the only instance of a large heavy water detector and deserves mention here. In addition to an outer 1.7 kton of light water, SNO contained 1 kton of $\mathrm{D_2O}$, giving it unique sensitivity to neutrino neutral current ($\nu_x + d \rightarrow \nu_x + p + n$), and charged current ($\nu_e + d \rightarrow p + p + e^-$) deuteron breakup reactions. The neutrons were detected in three ways: In the first phase, via the reaction $n + d \rightarrow t + \gamma + 6.25$ MeV; Cherenkov radiation from electrons Compton-scattered by the γ rays was observed. In the second phase, NaCl was dissolved in the water. ^{35}Cl captures neutrons, $n + {}^{35}\mathrm{Cl} \rightarrow {}^{36}\mathrm{Cl} + \gamma + 8.6$ MeV. The γ rays were observed via Compton scattering. In a final phase, specialized low-background ^{3}He counters ("neutral current detectors" or NCDs) were deployed in the detector. These counters detected neutrons via $n + {}^{3}\mathrm{He} \rightarrow p + t + 0.76$ MeV; ionization charge from energy loss of the products was recorded in proportional counters.

35.3.2. *Neutrino telescopes* :

Revised Aug. 2017 by Ch. Spiering (DESY/Zeuthen) and U.F. Katz (Univ. Erlangen)

The primary goal of neutrino telescopes (NTs) is the detection of astrophysical neutrinos, in particularly those which are expected to accompany the production of high-energy cosmic rays in astrophysical accelerators. NTs in addition address a variety of other fundamental physics issues like indirect search for dark matter, study of neutrino oscillations, search for exotic particles like magnetic monopoles or study of cosmic rays and their interactions [45,46,47].

NTs are large-volume arrays of "optical modules" (OMs) installed in open transparent media like water or ice, at depths that completely block the daylight. The OMs record the Cherenkov light induced by charged secondary particles produced in reactions of high-energy neutrinos in or around the instrumented volume. The neutrino energy, E_ν, and direction can be reconstructed from the hit pattern recorded. NTs typically target an energy range $E_\nu \gtrsim 100\,\mathrm{GeV}$; sensitivity to lower energies is achieved in dedicated setups with denser instrumentation.

In detecting cosmic neutrinos, three sources of backgrounds have to be considered: (i) *atmospheric neutrinos* from cosmic-ray interactions in the atmosphere, which can be separated from cosmic neutrinos on a statistical basis, or, for down-going neutrinos, by vetoing accompanying muons; (ii) down-going punch-through *atmospheric muons* from cosmic-ray interactions, which are suppressed by several orders of magnitude with respect to the ground level due to the large detector depths. They can be further reduced by selecting upward-going or high-energy neutrinos or by self-veto methods; (iii) random backgrounds due to photomultiplier (PMT) dark counts, ^{40}K decays (mainly in sea water) or bioluminescence (only water), which impact adversely on event recognition and reconstruction. Note that atmospheric neutrinos and muons allow for investigating neutrino oscillations and cosmic ray anisotropies, respectively.

Recently, it has become obvious that a precise measurement of the energy-zenith-distribution of atmospheric neutrinos may allow for determining the neutrino mass hierarchy by exploiting matter-induced oscillation effects in the Earth [48,49].

Neutrinos can interact with target nucleons N through charged current ($\overset{(-)}{\nu}_\ell N \rightarrow \ell^\mp X$, CC) or neutral current ($\overset{(-)}{\nu}_\ell N \rightarrow \overset{(-)}{\nu}_\ell X$, NC) processes. A CC reaction of a $\overset{(-)}{\nu}_\mu$ produces a muon track and a hadronic particle cascade, whereas all NC reactions and CC reactions of $\overset{(-)}{\nu}_e$ produce particle cascades only. CC interactions of $\overset{(-)}{\nu}_\tau$ can have either signature, depending on the τ decay mode. In most astrophysical models, neutrinos are expected to be produced through the $\pi/K \to \mu \to e$ decay chain, *i.e.*, with a flavour ratio $\nu_e : \nu_\mu : \nu_\tau \approx 1 : 2 : 0$. For sources outside the solar system, neutrino oscillations turn this ratio to $\nu_e : \nu_\mu : \nu_\tau \approx 1 : 1 : 1$ upon arrival on Earth.

The total neutrino-nucleon cross section is about $10^{-35}\,\mathrm{cm}^2$ at $E_\nu = 1\,\mathrm{TeV}$ and rises roughly linearly with E_ν below this energy and as $E_\nu^{0.3-0.5}$ above, flattening out towards high energies. The CC:NC cross-section ratio is about 2:1. At energies above some TeV, neutrino absorption in the Earth becomes noticeable; for vertically upward-moving neutrinos (zenith angle $\theta = 180^\circ$), the survival probability is $74\,(27, < 2)\%$ for $10\,(100, 1000)$ TeV. On average, between 50% (65%) and 75% of E_ν is transfered to the final-state lepton in neutrino (antineutrino) reactions between 100 GeV and 10 PeV.

The final-state lepton follows the initial neutrino direction with a RMS mismatch angle $\langle \phi_{\nu\ell} \rangle \approx 1.5^\circ / \sqrt{E_\nu\,[\mathrm{TeV}]}$, indicating the intrinsic kinematic limit to the angular resolution of NTs. For CC $\overset{(-)}{\nu}_\mu$ reactions at energies above about 10 TeV, the angular resolution is dominated by the muon reconstruction accuracy of a few times 0.1° at most. For muon energies $E_\mu \gtrsim 1\,\mathrm{TeV}$, the increasing light emission due to radiative processes allows for reconstructing E_μ from the measured dE_μ/dx with an accuracy of $\sigma(\log E_\mu) \approx 0.3$; at lower energies, E_μ can be estimated from the length of the muon track if it is contained in the detector. These properties make CC $\overset{(-)}{\nu}_\mu$ reactions the prime channel for the identification of individual astrophysical neutrino sources.

Hadronic and electromagnetic particle cascades at the relevant energies are 5–20 m long, *i.e.*, short compared to typical OM distances. The total amount of Cherenkov light provides a direct measurement of the cascade energy with an accuracy of about 20% at energies above 10 TeV and 10% beyond 100 TeV for events contained in the instrumented volume. Neutrino flavour and reaction mechanism can, however, hardly be determined and neutrinos from NC reactions or τ decays may carry away significant “invisible” energy. Above 100 TeV, the average directional reconstruction accuracy of cascades is 10–15 degrees in polar ice and better than 2 degrees in water, the difference being due to the inhomogeneity of the ice and stronger light scattering in ice. These features, together with the small background of atmospheric $\overset{(-)}{\nu}_e$ and $\overset{(-)}{\nu}_\tau$ events, makes the cascade channel particularly interesting for searches for a diffuse, high-energy excess of extraterrestrial over atmospheric neutrinos. In water, cascade events can also be used for the search for point sources of cosmic neutrinos, albeit the inferior angular accuracy compared to muon tracks leads to a higher background from atmospheric neutrinos.

The detection efficiency of a NT is quantified by its effective area, *e.g.*, the fictitious area for which the full incoming neutrino flux would be recorded (see Fig. 35.5). The increase with E_ν is due to the rise of neutrino cross section and muon range, while neutrino absorption in the Earth causes the decrease at large θ. Identification of downward-going neutrinos requires strong cuts against atmospheric muons, hence the cut-off towards low E_ν. Due to the small cross section, the effective area is many orders of magnitude smaller than the geometrical dimension of the detector; a $\overset{(-)}{\nu}_\mu$ with 1 TeV can, *e.g.*, be detected with a probability of the order 10^{-6} if the telescope is on its path.

Detection of upward-going muons allows for identifying neutrino interactions far outside the instrumented volume. This method, however, is only sensitive to CC $\overset{(-)}{\nu}_\mu$ interactions

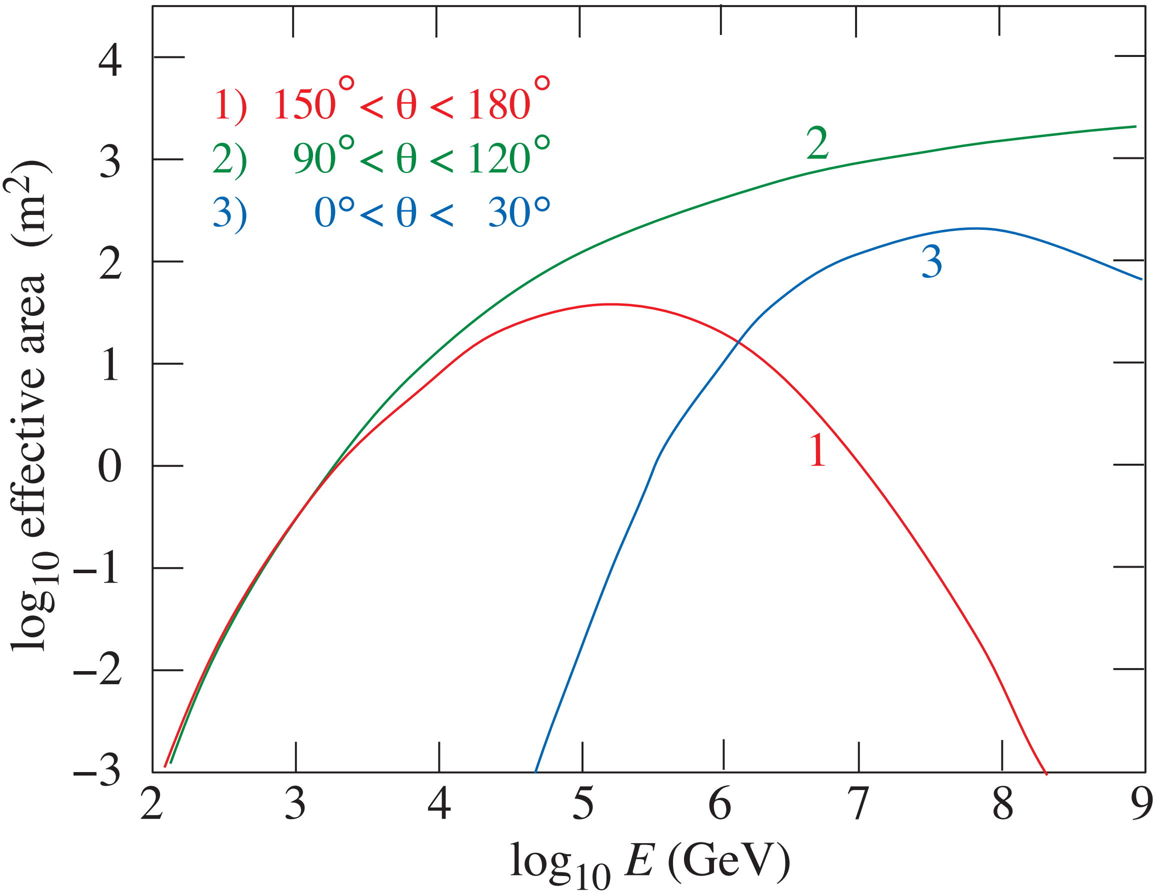

Figure 35.5: Effective $\overleftrightarrow{\overline{\nu}}_\mu$ area for IceCube as an example of a cubic-kilometre NT, as a function of neutrino energy for three intervals of the zenith angle θ. The values shown here correspond to a specific event selection for point source searches.

and cannot be extended to more than 5–10 degrees above the geometric horizon, where the background of atmospheric muons becomes prohibitive. Alternatively, one can select events that start inside the instrumented volume and thus remove incoming muons that generate early hits in the outer layers of the detector. Such a veto-based event selection is sensitive to neutrinos of all flavours from all directions, albeit with a reduced efficiency since a part of the instrumented volume is sacrificed for the veto. Such a muon veto, or vetoing events with a coincident signal in the surface array, also rejects down-going atmospheric neutrinos that are accompanied by muons from the same air shower and thus reduces the atmospheric-neutrino background. Actually, the breakthrough in detecting high-energy cosmic neutrinos has been achieved with this technique.

Note that the fields of view of NTs at the South Pole and in the Northern hemisphere are complementary for each reaction channel and neutrino energy.

35.3.2.1. *The Projects:*

Table 35.3: Past, present and future neutrino telescope projects and their main parameters. The milestone years give the times of project start, of first data taking with partial configurations, of detector completion, and of project termination. Projects with first data expected past 2020 are indicated in italics. The size refers to the largest instrumented volume reached during the project development. See [47] for references to the different projects where unspecified.

Experiment	Milestones	Medium/ Location	Size (km^3)	Remarks
DUMAND	1978/–/–/1995	Pacific/Hawaii		Terminated due to technical/funding problems
NT-200	1980/1993/1998/2015	Lake Baikal	10^{-4}	First proof of principle
GVD [50]	2012/2015/–/–	Lake Baikal	0.5–1.5	High-energy ν astronomy, first 2 clusters installed
NESTOR	1991/–/–/–	Med. Sea		2004 data taking with prototype
NEMO	1998/–/–/–	Med. Sea		R&D project, prototype tests
AMANDA	1990/1996/2000/2009	Ice/South Pole	0.015	First deep-ice neutrino telescope
ANTARES	1997/2006/2008/–	Med. Sea	0.010	First deep-sea neutrino telescope
IceCube	2001/2005/2010/–	Ice/South Pole	1.0	First km^3-sized detector
IceCube-Gen2 [51]	2014/–/–/–	Ice/South Pole	5–10	Planned extension of IceCube covering low and high energies, a surface array and radio detection
KM3NeT/ARCA [49]	2013/(2015)/–/–	Med. Sea	1–2	First construction phase started
KM3NeT/ORCA [49]	2014/(2017)/–/–	Med. Sea	0.003	Low-energy configuration for neutrino mass hierarchy
KM3NeT Phase 3	2013/–/–/–	Med. Sea	3–6	6 building blocks + ORCA

35.3.2.2. *Properties of media:*

The efficiency and quality of event reconstruction depend strongly on the optical properties (absorption and scattering length, intrinsic optical activity) of the medium in the spectral range of bialkali photocathodes (300–550 nm). Large absorption lengths result in a better light collection, large scattering lengths in superior angular resolution. Deep-sea sites typically have effective scattering lengths of > 100 m and, at their peak transparency around 450 nm, absorption lengths of 50–65 m. The absorption length for Lake Baikal is 22–24 m. The properties of South Polar ice vary strongly with depth; at the peak transparency wave length (400 nm), the scattering length is between 5 and 75 m and the absorption length between 15 and 250 m, with the best values in the depth region 2200–2450 m and the worst ones in the layer 1950–2100 m.

Noise rates measured by 25 cm PMTs in deep polar ice are about 0.5 kHz per PMT and almost entirely due to radioactivity in the OM components. The corresponding rates in sea water are typically 60 kHz, mostly due to ^{40}K decays. Bioluminescence activity can locally cause rates on the MHz scale for seconds; the frequency and intensity of such "bursts" depends strongly on the sea current, the season, the geographic location, and the detector geometry. Experience from ANTARES shows that these backgrounds are manageable without a major loss of efficiency or experimental resolution.

35.3.2.3. *Technical realisation:*

Optical modules (OMs) and PMTs: An OM is a pressure-tight glass sphere housing one or several PMTs with a time resolution in the nanosecond range, and in most cases also electronics for control, HV generation, operation of calibration LEDs, time synchronisation and signal digitisation.

Hybrid PMTs with 37 cm diameter have been used for NT-200, conventional hemispheric PMTs for AMANDA (20 cm) and for ANTARES, IceCube and Baikal-GVD (25 cm). A novel concept has been chosen for KM3NeT. The OMs (43 cm) are equipped with 31 PMTs (7.5 cm), plus control, calibration and digitisation electronics. The main advantages are that (i) the overall photocathode area exceeds that of a 25 cm PMT by more than a factor of 3; (ii) the individual readout of the PMTs results in a very good separation between one- and two-photoelectron signals which is essential for online data filtering and random background suppression; (iii) the hit pattern on an OM provides directional information; (iv) no mu-metal shielding against the Earth magnetic field is required. Figure 35.6 shows the OM designs of IceCube and KM3NeT.

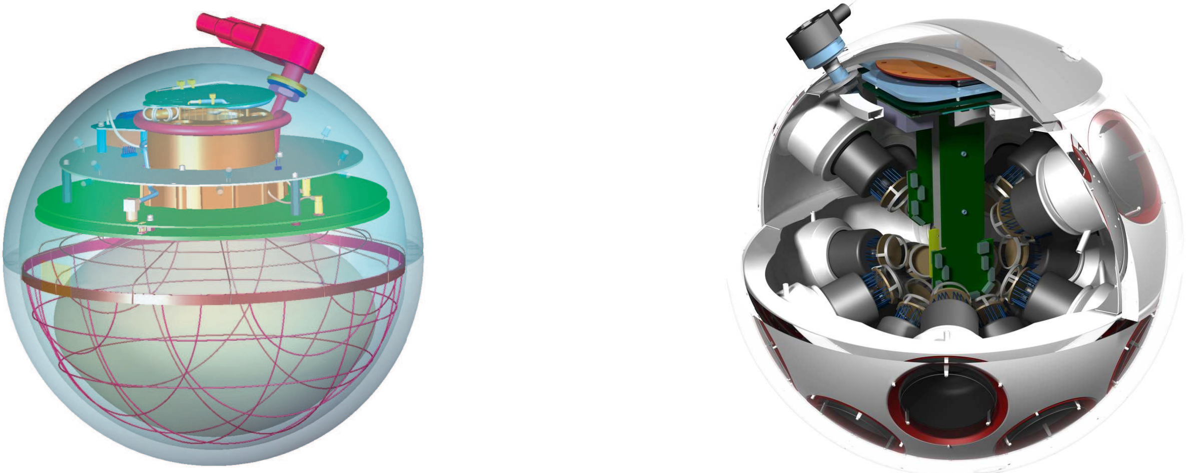

Figure 35.6: Schematic views of the digital OMs of IceCube (left) and KM3NeT (right).

Readout and data filtering: In current NTs the PMT data are digitised in situ, for ANTARES and Baikal-GVD in special electronics containers close to the OMs, for IceCube and KM3NeT inside the OMs. For IceCube, data are transmitted via electrical cables of up to 3.3 km length, depending on the location of the strings and the depth of the OMs; for ANTARES, KM3NeT and Baikal-GVD optical fibre connections have been chosen (several 10 km for the first two and 4 km for GVD).

The full digitised waveforms of the IceCube OMs are transmitted to the surface for pulses appearing in local coincidences on a string; for other pulses, only time and charge information is provided. For ANTARES (time and charge) and KM3NeT (time over threshold), all PMT signals above an adjustable noise threshold are sent to shore.

The raw data are subsequently processed on online computer farms, where multiplicity and topology-driven filter algorithms are applied to select event candidates. The filter output data rate is about 10 GByte/day for ANTARES and of the order 1 TByte/day for IceCube (100 GByte/day transfered via satellite) and KM3NeT.

Calibration: For efficient event recognition and reconstruction, the OM timing must be synchronised at the few-nanosecond level and the OM positions and orientations must be known to a few 10 cm and a few degrees, respectively. Time calibration is achieved by sending synchronisation signals to the OM electronics and also by light calibration signals emitted at known times by LED or laser flashers emitted in situ (ANTARES, KM3NeT). Precise position calibration is achieved by measuring the travel time of light calibration signals sent from OM to OM (IceCube) or acoustic signals sent from transducers at the sea floor to receivers on the detector strings (ANTARES, KM3NeT, Baikal-GVD). Absolute pointing and angular resolution can be determined by measuring the "shadow of the moon" (*i.e.*, the directional depletion of muons generated in cosmic-ray interactions). IceCube has shown that both are below 1°, confirming MC calculations which indicate a precision of $\approx 0.5^\circ$ for energies above 10 TeV. For KM3NeT, simulations indicate that sub-degree precision in the absolute pointing can be reached within a few weeks of operation.

Detector configurations: IceCube (see Fig. 35.7) consists of 5160 Digital OMs (DOMs) installed on 86 strings at depths of 1450 to 2450 m in the Antarctic ice; except for the DeepCore region, string distances are 125 m and vertical distances between OMs 17 m. 324 further DOMs are installed in IceTop, an array of detector stations on the ice surface above the strings. DeepCore is a high-density sub-array at large depths (*i.e.*, in the best ice layer) at the centre of IceCube.

The NT200 detector in Lake Baikal at a depth of 1100 m consisted of 8 strings attached to an umbrella-like frame, with 12 pairs of OMs per string. The diameter of the instrumented volume was 42m, its height 70 m. Meanwhile (2017), the Baikal collaboration has installed the first two clusters of a future cubic-kilometre array. A first phase, covering a volume of about 0.4 km^3, will consist of 8 clusters, each with 288 OMs at 8 strings; its completion is scheduled for 2020. A next stage could comprise about 20 clusters and cover up to 1.5 km^3.

ANTARES comprises 12 strings with lateral distances of 60–70 m, each carrying 25 triplets of OMs at vertical distances of 14.5 m. The OMs are located at depths 2.1–2.4 km, starting 100 m above the sea floor. A further string carries devices for calibration and environmental monitoring. A system to investigate the feasibility of acoustic neutrino detection is also implemented.

KM3NeT will consist of building blocks of 115 strings each, with 18 OMs per string. Prototype operations have successfully verified the KM3NeT technology [52]. In the

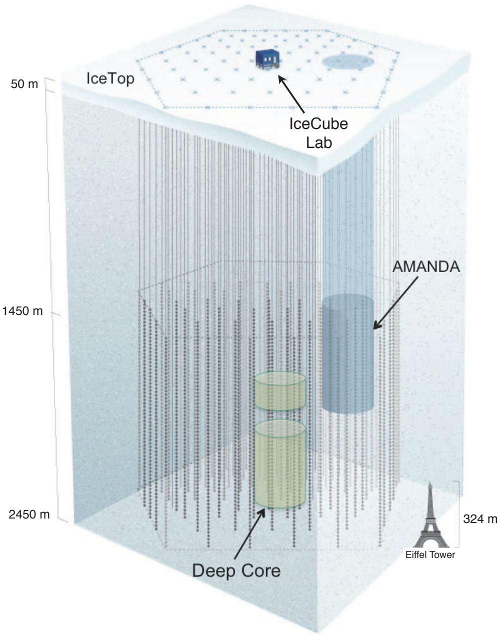

Figure 35.7: Schematic view of the IceCube neutrino observatory comprising the deep-ice detector including its nested dense part DeepCore, and the surface air shower array IceTop. The IceCube Lab houses data acquisition electronics and the computer farm for online processing. Operation of AMANDA was terminated in 2009.

upcoming phase 2.0 of its staged implementation, KM3NeT aims at two building blocks for neutrino astronomy, with vertical distances between OMs of 36 m and a lateral distance between adjacent strings of 90 m (ARCA, for *Astroparticle Research with Cosmics in the Abyss*) and at one block for the measurement of the neutrino mass hierarchy, with vertical distances between OMs of 9 m and a lateral distance between adjacent strings of about 20 m (ORCA, for *Oscillation Research with Cosmics in the Abyss*) [49]. A first installation phase of ARCA near Capo Passero, East of Sicily and of ORCA near Toulon has started in 2015 and comprises 24 (7) ARCA (ORCA) strings to be deployed by end of 2018. Completion of the full three blocks is expected for 2021.

35.3.2.4. *Results:*

Atmospheric neutrino fluxes have been precisely measured with AMANDA and ANTARES ($\overset{(-)}{\nu}_\mu$) and with IceCube ($\overset{(-)}{\nu}_\mu$, $\overset{(-)}{\nu}_e$); the results are in agreement with predicted spectra. No astrophysical point sources have been identified yet, and no indications of neutrino fluxes from dark matter annihilations or of exotic phenomena have been found (see [47] and references therein). IceCube has furthermore reported an energy-dependent anisotropy of cosmic-ray induced muons.

In 2013, an excess of track and cascade events between 30 TeV and 1 PeV above background expectations was reported by IceCube; this analysis used the data taken in 2010 and 2011 and for the first time employed containment conditions and an atmospheric muon veto for suppression of down-going atmospheric neutrinos (High-Energy Starting Event analysis, HESE). A display of one of the selected events is shown in Fig. 35.8.

The observed excess reached a significance of 5.7σ in a subsequent analysis of 3 years of data [53] and cannot be explained by atmospheric neutrinos and misidentified atmospheric muons alone. Some clustering of the HESE events close to the Galactic Centre was observed. The hypothesis that this low-significance excess could be due to a point source with a spectral index of ≥ 2 was constrained by an analysis of ANTARES data looking at lower energies and with superior pointing to the same sky region [54]. In a six-year HESE sample, combined with a sample of high-energy through-going muons, the mentioned excess close to the Galactic Centre has essentially disappeared (see Fig. 35.9). Meanwhile the energy range of the IceCube HESE analysis has been extended down to 1 TeV and the high-energy excess confirmed; also, events with through-going muons showed a corresponding excess of cosmic origin. In [55], the various analyses have been combined. Assuming the cosmic neutrino flux to be isotropic, flavour-symmetric and ν-$\overline{\nu}$-symmetric at Earth, the all-flavour spectrum is well described by a power law with normalisation $6.7^{+1.1}_{-1.2} \times 10^{-18}\,\mathrm{GeV}^{-1}\mathrm{s}^{-1}\mathrm{sr}^{-1}\mathrm{cm}^{-2}$ at 100 TeV and a spectral index -2.50 ± 0.09 for energies between 25 TeV and 2.8 PeV. A spectral index of -2, an often quoted benchmark value, is disfavoured with a significance of 3.8σ.

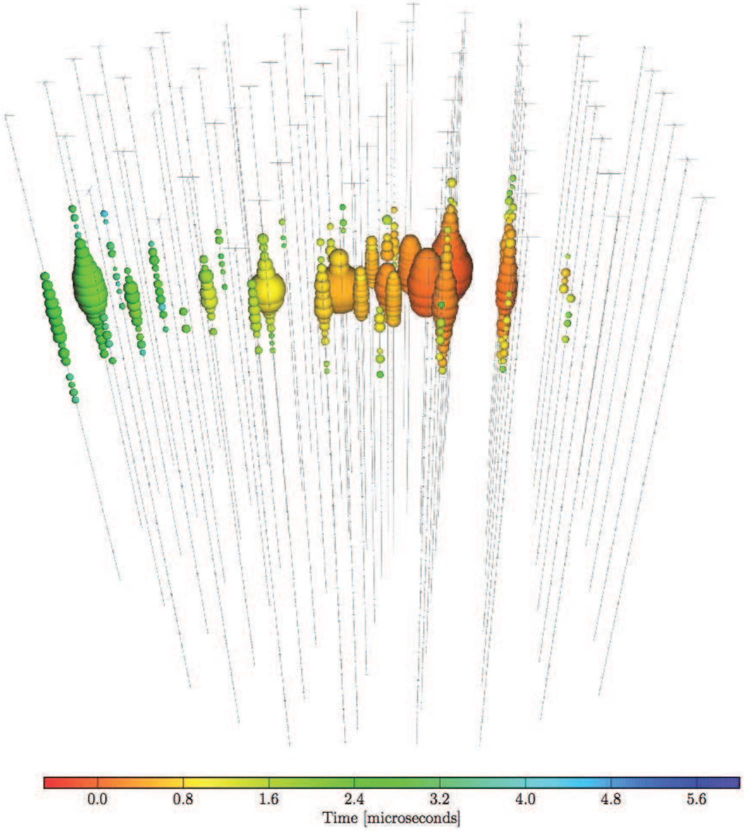

Figure 35.8: Event display of one of the starting-track events from [53]. The deposited energy is 70 TeV, the colour code indicates the signal timing (red: early; green: late).

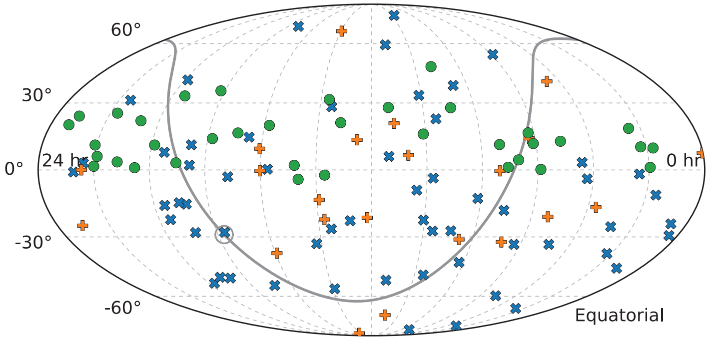

Figure 35.9: Arrival directions of IceCube candidate events for cosmic neutrinos in equatorial coordinates. The plot contains 82 HESE events, with shower-like events marked as blue × and muon tracks as orange +, and in addition 36 through-going muons tracks with an energy deposit exceeding 200 TeV (green circles). Approximately 40% of the events are expected to originate from atmospheric backgrounds. The grey curve denotes the Galactic Plane and the grey circle the Galactic Centre (from [58]) .

At lower energies, down to 10 GeV, IceCube/DeepCore and ANTARES have identified clear signals of oscillations of atmospheric neutrinos. The closely spaced OMs of DeepCore allow for selecting a very pure sample of low-energy $\overset{(-)}{\nu}_\mu$ (6–56 GeV) that produce upward moving muons inside the detector. The neutrino energy is determined from the energy of the hadronic shower at the vertex and the muon range. Fits to the energy/zenith-dependent deficit of muon neutrinos provide constraints on the oscillation parameters $\sin^2\theta_{23}$ and Δm^2_{23} (see Fig. 14.13 in "Neutrino masses, mixing, and oscillations" review).

See [56] and [57] for summaries of recent results of IceCube and ANTARES, respectively.

35.3.2.5. *Plans beyond 2020:*

Within the future IceCube-Gen2 project, it is planned to extend the sensitivity of IceCube towards both lower and higher energies. A substantially denser instrumentation of a sub-volume of DeepCore would lead to an energy threshold for neutrino detection of a few GeV (PINGU project, aiming primarily at measuring the neutrino mass hierarchy). For higher energies, a large-volume extension, combined with a powerful surface veto, is envisaged [7]. A very first phase with 7 closely spaced strings is discussed, aiming to cover part of the PINGU program, to better calibrate the existing IceCube and to test new technologies. More information on the future extensions of GVD and KM3NeT are given above, in Table 35.3 and in [49].

35.3.3. *Coherent radio Cherenkov radiation detectors* :

Revised August 2017 by S.R. Klein (LBNL/UC Berkeley)

Radio-frequency (RF) pulses are an attractive signature for coherent Cherenkov radiation from showers produced from interactions of ultra-high energy cosmic neutrinos. RF detectors can be used to search for energetic neutrinos from three types of sources: astrophysical objects (*i.e.* extending measurements the neutrino energy spectrum observed at TeV to PeV energies upward in energy, searching for 'GZK' neutrinos associated with cosmic-ray-cosmic microwave background radiation interactions, and searching for neutrinos from beyond-standard-model physics. These types are roughly associated with energies below 10^{18} eV, the energy range 10^{18} to 10^{20} eV, and above 10^{20} eV. GZK neutrinos are produced when protons with energy $E > 4 \times 10^{19}$ eV interact with cosmic microwave background radiation (CMB) and are excited to a Δ^+ resonance. The subsequent $\Delta^+ \rightarrow n\pi^+$ decay leads to the production of neutrinos with energies above 10^{18} eV [59]. Neutrinos are the only long-range probe of the ultra-high energy cosmos, because protons, heavier nuclei and photons with energies above 5×10^{19} eV are limited to ranges of less than 100 Mpc by interactions with the CMB and early starlight.

To detect a GZK neutrino signal of at least a few events per year (assuming that ultra-high energy cosmic-rays are protons) requires a detector with an active volume of about 100 km^3, made out of a non-conducting solid (or potentially liquid) medium, with a long absorption length for radio waves. The huge volumes require that this be a common material. A dense medium would be ideal to reduce the detector volume, but, unfortunately, the available natural media have only moderate density. Optical Cherenkov and acoustical detectors are limited by short ($<$ 300 m) attenuation lengths [60] so would require a prohibitive number of sensors. Radio-detection is the only current approach that can scale to this volume. Table 35.4 compares the characteristics of commonly used media - the lunar regolith and several locations on the polar ice pack [61].

Electromagnetic and hadronic showers produce radio pulses via the Askaryan effect [62], as discussed in Sec. 33. The shower contains more electrons than positrons, leading to coherent emission.

High-frequency radiation is concentrated around the Cherenkov angle. On the cone, the electric field strength, $E_{\rm ch}$ at a frequency f from an electromagnetic shower from a ν_e may be roughly parameterized as [63]

$$E_{\rm Ch}(V/{\rm MHz}) = 2.53 \times 10^{-7} \frac{E_\nu}{1{\rm TeV}} \frac{f}{f_c} \left[\frac{1}{1 + (f/f_c)^{1.44}} \right]. \tag{35.3}$$

The electric field strength increases linearly with frequency, up to a cut-off f_c, which is set by the transverse size of the shower [64]. The maximum wavelength is roughly the Moliere radius divided by $\cos(\theta_C)$ where θ_C is the Cherenkov angle. Some examples are given in Table 35.4.

Near f_c, radiation is narrowly concentrated around the Cherenov angle [64]. At lower frequencies, the limited length of the emitting region leads to a broadening in emission angle around the Cherenkov cone. Away from θ_C, the electric field from Eq. (35.3) is reduced by [63],

$$\frac{E}{E_{\rm Ch}} = \exp\left(-\frac{1}{2} \frac{(\theta - \theta_C)^2}{(2.2^0 \times [1{\rm GHz}/f])^2} \right), \tag{35.4}$$

At very low frequencies, the distribution is nearly isotropic.

Along the Cherenkov cone, the initial pulse width is $\approx$ 1 nsec, but it may be broadened by dispersion as it propagates, particularly for signals from the Moon traversing the ionosphere. As long as the dispersion can be compensated for, a large bandwidth detector

Table 35.4: Characteristics of different detection media for radio-Cherenkov signals. The attenuation length is at a frequency of 300 MHz; the Greenland figure is extrapolated upward from the 75 MHz measurements. The lunar regolith and ice have similar Cherenkov angles because they have similar indices of refraction.

Medium	Density	Cherenkov Ang.	Cutoff Freq.	Atten. Length
Lunar Regolith	2.5 g/cm^3	56^0	3.0 GHz	9m/f(GHz) [61]
Antarctic Ice (South Pole)	0.92 g/cm^3	56^0	1.15 GHz	900 m [65]
Ross Ice Shelf	0.92 g/cm^3	56^0	1.15 GHz	406 m [66]
Greenland	0.92 g/cm^3	56^0	1.15 GHz	1022 m [67]

is the most sensitive. Spectral information can be used to reject background, and to help reconstruct the neutrino direction, because the cutoff frequency depends on the observation angle (with respect to the Cherenkov cone).

The electric field is linearly proportional to the neutrino energy, so the power (field strength squared) is proportional to the square of the neutrino energy. Since the signal is a radio wave, the field amplitude decreases as $1/R$, plus absorption in the intervening medium. The detection threshold is determined by the distance to the antenna and the noise characteristics of the detector. For an antenna located in the detection medium, the typical threshold is around 10^{17} eV; for stand-off (remote sensing) detectors, the threshold rises roughly linearly with the distance. These thresholds can be reduced significantly by using directional antennas and/or combining the signals from multiple antennas using beam-forming techniques. Experiments have used both approaches to reduce trigger-level noise, or to reject background at the analysis level. For multi-element arrays, the threshold drops as the square root of number of antennas, since the signal adds in-phase while the backgrounds add with random phases [68].

The main background sources are anthropogenic noise, antenna/preamp noise, cosmic-ray air showers, charge generated by blowing snow, and lightning. The need to limit anthropogenic noise has led most experimental groups to select remote locations for their detectors.

The signal is linearly polarized in the plane perpendicular to the neutrino direction. This polarization is an important check that any observed signal is indeed coherent Cherenkov radiation. Polarization measurements can be used to help reconstruct the neutrino direction.

At energies above 10^{20} eV, the Landau-Pomeranchuk-Migdal effect significantly spreads out electromagnetic showers, producing what are effectively subshowers with significant separation. The radio emission becomes even more concentrated around the Cherenkov cone, and then, at higher energies the emission begins to vary event-by-event. Because of this, many of the experiments that study higher energy neutrinos focus on the hadronic shower from the struck nucleus. This contains on average only about 20% of the energy, but with large fluctuations. The hadronic shower is useful for very high energy searches ($\gg 10^{20}$ eV) because it is much less subject to the LPM effects.

Radio detectors have observed cosmic-ray air showers in the atmosphere. The physics of radio-wave generation in air showers is more complex because of the large contribution due to charge separation as electrons and positrons bend in different directions as they propagate, leading to a growing charge dipole (transverse current) [69]. This time-varying transverse current emits radiation, spread over the transverse size of the shower. Since the radiating particles are moving relativistically downward, a ground-based observer sees a Lorentz contracted pulse which can have frequency components reaching the GHz range, limited by the thickness of the particle shower. There is also a contribution from geosynchrotron radiation, as $e^{\pm}$ are bent in the same field [69]. Coherent Cherenkov radiation is less important than these other sources. Experiments for ν detection may also detect air showers [70], which is also a potential background. Magnetic monopoles would also emit radio waves, and neutrino experiments have also set monpole flux limits [71].

35.3.4. *The Moon as a target* :

Because of its large size and non-conducting regolith, and the availability of large radio-telescopes, the Moon is an attractive target [72]. TableMoonList lists some lunar experiments. Conventional radio-telescopes are quite well suited to lunar neutrino searches, with natural beam widths not too dissimilar from the size of the Moon. Still, there are experimental challenges. The composition of the lunar regolith is not well known, and the attenuation length for radio waves must be estimated. The big limitation of lunar experiments is that the 240,000 km target-antenna separation leads to neutrino energy thresholds above 10^{20} eV.

Table 35.5: Experiments that have set limits on neutrino interactions in the Moon; current limits are shown in Fig. 1 of [61], with Lunaska (2015) from [73].

Experiment	Year	Dish Size	Frequency	Bandwidth	Obs. Time
Parkes	1995	64 m	1425 MHz	500 MHz	10 hrs
Glue	1999+	70 m, 34 m	2200 MHz	40-150 MHz	120 hrs
NuMoon	2008	11×25 m	115–180 MHz	—	50 hrs
Lunaska	2008	3× 22 m	1200–1800 MHz	—	6 nights
Lunaska	2015	64	1200-1500 MHz	300 MHz	127 hours
Resun	2008	4× 25 m	1450 MHz	50 MHz	45 hours

The effective volume probed by experiments depends on the geometry, which itself depends on the frequency range used. At high frequencies f, the electric field strength is high, leading to a lower energy threshold, but the sensitive volume is limited because the Cherenkov cone only points toward the Earth for a narrow range of geometries. Lower frequency radiation is more isotropic, so the effective volume is larger, but, because the electric field is weaker, the energy threshold is higher. The $1/f$ dependence of the attenuation length in the lunar regolith further increases the effective volume at low frequencies.

With modern technology, it is increasingly viable to search over very broad frequency ranges [74]. One technical challenge is due to dispersion (frequency dependent time delays) in the ionosphere. Dispersion can be largely removed with a de-dispersion filter, using either analog circuitry or post-collection digital processing.

Lunar experiments use different techniques to reduce the anthropogenic background. Some experiments use multiple antennas, separated by at least hundreds of meters; by requiring a coincidence within a small time window, anthropogenic noise can be rejected. With good enough timing, beam-forming techniques can be used to further reduce the background. An alternative approach is to use beam forming with multiple feed antennas viewing a single reflector, to ensure that the signal points back to the moon.

In the near future, several large radio detector arrays should reach significantly lower limits. The LOFAR array is beginning to take data with 36 detector clusters spread over Northwest Europe. In the longer term, the Square Kilometer Array (SKA) with 1 km^2 effective area will push thresholds down to near 10^{20} eV [74].

35.3.5. *Ice-based detectors* :

Lower energy thresholds require a smaller antenna-target separation. Natural ice is an attractive medium for this, with attenuation lengths over 300 m. The attenuation length varies with the frequency and ice temperature, with higher attenuation in warmer ice. Table 35.4 lists some radio attenuation measurements.

Although ice is mostly uniform, the top $\approx$ 100 m of Antarctic ice, the 'firn,' exhibits a gradual transition from packed snow at the surface (typical density 0.35 g/cm^3) to solid ice (density 0.92 g/cm^3) below [75]. The index of refraction depends linearly on the density, so radio waves curve downward in the firn. This bending reduces the effectiveness of surface or aerial antennas. The thickness of the firn varies with location; it is thicker in central Antarctica than in the coastal ice sheets. For aerial observations, the surface roughness of the ice can affect signals as they transition from the ice to the atmosphere. There are also indications that the increase in firn density is non-monotonic. This can lead to a non-monotonic change in index of refraction which may create waveguides which trap and propagate waves horizontally [76].

There are two types of Antarctic neutrino experiments. In one class, antennas mounted on scientific balloons observe the ice from above. The ANITA experiment is one example. It has made four flights around Antarctica, floating at an altitude around 35 km [77]. Its 32/40/48 (depending on the flight) dual-polarization horn antennas scanned the surrounding ice, out to the horizon (650 km away). Because of the small angle of incidence, ANITA could make use of polarization information; ν signals should be vertically polarized, while most background from cosmic-ray air showers is expected to be horizontally polarized.

Because of the significant source-detector separation, ANITA is most sensitive at energies above 10^{19} eV, above the peak of the GZK neutrino spectrum. As with the lunar experiments, ANITA had to contend with anthropogenic backgrounds. The ANITA collaboration uses their multiple antennas as a phased array to achieve good pointing accuracy, and used that to remove all apparent signals that pointed toward known or suspected areas of human habitation. By using the several-meter separation between antennas, they achieved a pointing accuracy of 0.2-0.4^0 in elevation, and 0.5-1.1^0 in azimuth. ANITA has set the most stringent limits on GZK neutrinos to date.

The proposed EVA experiment will use a portion of a fixed-shape balloon as a large parabolic radio antenna. Because of the large antenna surface, they hope to achieve threshold around 10^{17} eV.

Other ice based experiments use antennas located within the active volume, allowing them to reach thresholds around 10^{17} eV. This approach was pioneered by the RICE experiment [78], which buried 18 half-wave dipole antennas in holes drilled for AMANDA at the South Pole, at depths from 100 to 300 m. The hardware was sensitive from 200 MHz to 1 GHz. Each antenna fed an in-situ preamplifier which transmitted the signals to surface digitizing electronics.

Two groups are have deployed prototype arrays, with the goal of a building a detector with a $\sim$100 km^3 active volume. In both concepts, the hardware is modular, so the detector volume scales roughly linearly with the available funding. The Askaryan Radio Array (ARA) is located at the South Pole [79], while the Antarctic Ross Iceshelf Antenna Neutrino Array (ARIANNA) is on the Ross Ice Shelf [80], about 110 km north of McMurdo station. Both experiments use multiple antennas, with varying degrees of connection. They use the timing between multiple antennas in a single station to determine the arrival direction, and have angular resolutions of a few degrees. At larger distance scales, such as between ARA and ARIANNA stations, the relative timing uncertainty is larger, and the stations are effectively independent, with independent triggers, and the data is only combined offline.

The two approaches have many differences. ARA [79] is located at the South Pole, where the ice is very cold and more than 2800 m thick, leading to long attenuation lengths and allowing a large active volume, while ARIANNA [80] is on the Ross Ice Shelf, about 110 km north of McMurdo station, where the ice is 575 m thick. The ice is warmer there, but it sits atop the Ross Sea. At the site, the ice-water interface is smooth, so it acts as a reflector for radio waves. These reflections give ARIANNA sensitivity to downward going neutrinos, and to more of the Cherenkov cone for horizontal neutrinos.

The two experiments have different antenna deployment schemes. ARA buries their antennas up to 200 m deep in the ice, to avoid radio wave refraction in the firn and give their antennas a clear field of view. However, drilling holes has costs, and the limited hole diameter (15 cm in ARA) requires compromises between antenna design (particularly for horizontally polarized waves), mechanical support, power and communications. In contrast, the ARIANNA antennas are placed in shallow holes. This greatly simplifies deployment and avoids limitations on antenna design, but at a cost of reduced sensitivity to neutrino interactions near the surface.

The current ARA proposal, ARA-37 [79], calls for an array of 37 stations, each consisting of 16 embedded antennas deployed in narrow boreholes 50-200 m deep. The antennas will detect signals from 150 to 850 MHz for vertical polarization, and 250 MHz to 850 MHz for horizontal polarization. ARA plans to use bicone antennas for vertical polarization, and quad-slotted cylinders for horizontal polarization. The collaboration uses notch filters and surface veto antennas to eliminate most anthropogenic noise, and vetos events when aircraft are in the area, or weather balloons are being launched. Each ARIANNA station (1296 have been proposed) [80] will include multiple log-periodic dipole antennas sensitive to the frequency range from about 80 MHz to 1 GHz. The multiple antennas allow for single-station directional and polarization measurements. A few of the antennas will point upward to help veto cosmic-ray air showers and other external backgrounds.

35.4. Large time-projection chambers for rare event detection

Revised Aug. 2017 by T. Shutt (SLAC).

Rare event searches require detectors that combine large target masses and low levels of radioactivity, and that are located deep underground to eliminate cosmic-ray related backgrounds. Past and present efforts include searches for the scattering of particle dark matter, neutrinoless double beta decay, and the measurement of solar neutrinos, while next generation experiments will also probe coherent scattering of solar, atmospheric and diffuse supernova background neutrinos. Large time project chambers (TPCs), adapted from particle collider experiments, have emerged as a leading technology for these efforts. Events are measured in a central region confined by a field cage and usually filled with a liquid noble element target. Ionized electrons are drifted (in the z direction) to an anode region by use of electrode grids and field shaping rings, where their magnitude and $x - y$ location is measured. In low background TPCs, scintillation generated at the initial event site is also measured, and the time difference between this prompt signal and the later-arriving charge signal gives the event location in z for a known electron drift speed. Thus, 3D imaging is a achieved in a monolithic central volume. Noble elements have relatively high light yields (comparable to or exceeding the best inorganic scintillators), and the charge signal can be amplified by multiplication or electroluminescence. Radioactive backgrounds are distinguished by event imaging, the separate measurements of charge and light, and scintillation pulse shape. For recent reviews of noble element detectors, see [81,82].

Methods for achieving very low radioactive backgrounds are discussed in general in section 34.6. The basic architecture of large TPCs is very favorable for this application because gas or liquid targets can be relatively easily purified, while the generally more radioactive readout and support materials are confined to the periphery. The 3D imaging of the TPC then allows self shielding in the target material, which is quite powerful when the target is large compared to mean scattering lengths of $\sim$ MeV neutrons and gammas from radioactivity ($\sim$ 10 cm in LXe, for example). The use of higher density targets (i.e., liquid instead of gas and/or higher mass elements) maximizes the ratio of target to surrounding material mass. The TPC geometry allows highly hermetic external shielding, with recent experiments using large water shields, in some cases enhanced with an active liquid scintillator layer.

In noble element targets, all non-noble impurities are readily removed (e.g., by chemical reaction in a commercial getter) so that only radioactive noble isotopes are a significant background concern. Xe, Ne and He have have no long lived radioactive isotopes (apart from the ^{136}Xe, discussed below). Kr has $\sim$ 1 MBq/kg of the beta emitter ^{85}Kr created by nuclear fuel reprocessing, making it unusable as a target, while the 1 Bq/kg level of the beta emitter ^{39}Ar is a nuisance for Ar-based experiments. Both of these can be backgrounds in other target materials, as can Rn emanating from detector components. Relatively low background materials are available for most of the structures surrounding the central target, with the exception of radioactive glasses and ceramics usually present in PMTs, feedthroughs and electrical components. Very low background PMTs with synthetic quartz windows, developed over the last decade, have been a key enabling technology for dark matter searches. These are not yet low enough in background for some double beta decay searches, which use radio-clean Si-based photon detectors.

An important technical challenge in liquid detectors is achieving the high voltages needed for electron drift and measurement. Quench gases which stabilize charge gain and speed electron transport in wire chambers cannot be used, since these absorb scintillation light (and also suppress charge extraction in dual-phase detectors, discussed below). At low energies (e.g., in a dark matter search) it is also important to suppress low-level emission of electrons and associated photons. Drift of electrons over meter scales with minimal loss from attachment on trace levels of dissolved impurities (e.g., O_2) has so far required continuous circulating purification. The relatively slow readout due to $\sim$ msec/m drift speeds is not a major pile-up concern in low background experiments.

35.4.1. *Dark matter and other low energy signals* :

A major goal of low background experiments is detection of WIMP (Weakly Interacting Massive Particle) dark matter through scattering on nuclei in a terrestrial detector (for a recent review, see [83]) . Energy transfers are generally small, a few tens of keV at most. Liquid noble TPCs distinguish nuclear recoils (NR) from dark matter from the usually dominant background of electron recoils (ER) from gamma rays and beta decays by requiring single scatters and based on their charge to light ratio or scintillation pulse shape, as described below. Neutrons are a NR background, but can be recognized in a large imaging TPC if they multiply scatter. To detect small charge signals, a dual phase technique is used wherein electrons from interactions in the liquid target are drifted to the liquid surface and extracted with high field ($\sim$ 5 kV/cm) into the gas phase leading to an amplified electroluminescence signal measured by an array of PMTs located just above. (Both charge multiplication and electroluminescence are possible in liquid, but have seen little use because the signals have very broad dispersion). This technique readily measures single electrons with $\sim$ cm $x - y$ resolution. The sides of the chamber are lined with highly (diffusively) reflective PTFE, and a second PMT array is located below the active volume to maximize the sensitivity to the initial scintillation signal.

The microscopic processes leading to signals in liquid nobles are complex. Energy deposited by an event generates pairs of free electron and ions, and also atoms in their lowest excited state. These rapidly form excimers which de-excite by emitting light. Excimers arise in both triplet and singlet states which have the same energy but different decay times. In an event track, some fraction of electrons recombine with ions, while the rest escape and are measured. Recombination leads to further excimer formation and hence more scintillation photons. Finally, some part of the energy is lost as heat - a small fraction for ER but a dominant and energy dependent fraction for NR. This complexity distinguishes ER and NR: for the same visible energy, the slower nuclear recoils form a denser track with less charge and more light than recoiling electrons, and they generate fewer long-lived triplet state scintillation photons than singlet-state photons. Charge and light yields depend on drift field, energy, and the initial particle (ER or NR), requiring extensive calibrations. The existing data has been incorporated into the NEST Monte Carlo framework. Typical yields are several tens of electrons and photons per keV of deposited energy (with up to 10-15 % efficiency for these photons being detected).

The scattering rates of WIMPs are model dependent, but are usually highest for spin-independent scattering which has an A^2 dependence, so that experiments to date have used LXe and LAr targets. LXe experiments have had the best WIMP sensitivity for all but the lowest most WIMP masses for the last decade, with the ton-scale XENON1T [84] and PANDAX-II [85] experiments now eclipsing LUX with world-leading results. Previous significant experiments also include XENON10/100, and ZEPLIN II/III. Next generation experiments under construction include LZ and XENONnT with roughly 7 tons active mass. If a dark matter signal is seen, its spin dependence could be probed with Xe targets isotopically separated into spin-rich and spin-poor targets.

The reach of LXe TPCs depends critically on the level of ER background rejection provided by the ratio of charge to light. Most reported values (at 50% NR acceptance) are near the 99.6% result obtained by LUX, while ZEPLIN III had 99.99%, possibly because of its very high drift field (4 kV/cm). While there is a basic framework [86] for how this improves with light collection and varies with electric field, a fully predictive understanding is not yet in hand. Pulse shape discrimination is present, but weak at low energy. The $\sim$ 178 nm scintillation light of Xe is just long enough to be transmitted through high purity synthetic quartz PMTs windows. Kr suppression to the $\sim$ ppt or better level is needed, and has been accomplished via distillation or chromatography.

Two experiments to date have produced dark matter limits using dual phase Ar TPCs: WARP and DarkSide-50, while ArDM is under development. A primary attraction of Ar compared to Xe is much lower raw material costs. However beta decays from ^{39}Ar, produced by cosmic-ray interactions in the atmosphere, give a low energy ER background roughly 10^8 times higher than the fundamental ER background from p-p solar neutrinos. Remarkably, however, pulse shape discrimination (PSD) of ER backgrounds is very powerful in LAr for sufficiently high energy, based on the favorably different ratio of populations of the singlet (6 ns lifetime) and triplet ($\sim 1.5\ \mu$ s lifetime) states. DarkSide has shown roughly 10^8 discrimination with $\geq 50\%$ WIMP acceptance above 47 keV. They have also extracted "aged" Ar with the 32.9 yr half-life ^{39} Ar reduced by a factor of 1400, via processing of underground (cosmic ray shielded) gas deposits. This lowers the energy threshold and allows ton-scale experiments without significant pile-up. Charge and light discrimination has also been demonstrated at high energy, but it is less well characterized than in LXe and appears weak at low energy. While the strong PSD in LAr allows relaxed requirements for ER backgrounds, U and Th contamination must still be kept very low because their decay chains create neutrons via (α, n) reactions, particularly in low Z elements such as PMT glass and PTFE. Waveshifter is used (typically TPB) because PMTs are blind to the 128 nm scintillation light.

LZ and XENONnT project sensitivity to WIMPs about a decade above the"floor" of coherent electron scattering of astrophysical neutrinos, which, absent a directional measurement (see below), are essentially indistinguishable from WIMPs. A 30-50 ton LXe TPC would approach the practical limit set by this floor for WIMP masses above $\sim$ 5 GeV if a $\sim$ 99.98% rejection (at 30% NR acceptance) of p-p solar ν ER backgrounds [87] is achieved, while a $\sim$ 200 ton LAr detector would achieve similar sensitivity for WIMPs above $\sim$ 50 GeV. Sensitivity to lower WIMP mass could be obtained by adding Ne to a LXe TPC, or, more speculatively,with a superfluid He TPC [88] read out with superconducting sensors (similar to the proposed HERON solar neutrino experiment). With sufficient control of dissolved Kr and especially Rn, the ER background in the next LXe experiments could be dominated by the poorly measured low energy spectrum of solar neutrinos from the main p-p burning reaction.

Measurement of NR recoil track direction would provide proof of the galactic origin of a dark matter signal since the prevailing WIMP direction varies on a daily basis as the earth spins. This cannot be achieved for the sub-micron tracks in any existing solid or liquid technology, but the mm-scale tracks in a low pressure gas (typically, $P \sim 50$ Torr) could be imaged with sufficiently dense instrumentation. Directionality can be established with $O(10^2)$ events by measuring just the track direction, while, with finer resolution that distinguishes the diffuse (dense) tail and dense (diffuse) head of NR (ER) tracks, only $O(10)$ events are required. Such imaging requires a high energy threshold, decreasing WIMP sensitivity, but also powerfully rejecting less dense ER background tracks.

A variety of TPC configurations are being pursued to accomplish this, most with a CF_4 target. The longest established effort, DRIFT, avoids diffusion washing out tracks for electron drift distances greater than ~ 20 cm by attaching electrons to CS_2, which drifts with vastly reduced diffusion. Other efforts drift electrons directly and use a variety of techniques for their measurement: DMTPC (electroluminescence + CCDs), MIMAC (MicroMegas), NEWAGE (GEMs), and D^3 (Si pixels). WIMP limits have been obtained by DRIFT, NEWAGE, and DMTPC. A related suggestion is that the amount of recombination in a high pressure Xe gas with an electron-cooling additive could be sensitive to the angle between the track and electric field [89], eliminating the need for track imaging. Directional measurements appear to be the only possibility to push beyond the floor of coherent neutrino scatters [90], though this would require extraodinarily large target mass.

35.4.2. $0\nu\beta\beta$ *Decay* :

Another major class of rare event search is neutrinoless double beta decay ($0\nu\beta\beta$). A limited set of nuclei are unstable against simultaneous beta decay of two neutrons. Observation of the lepton-number violating neutrinoless version of this decay would establish that neutrinos are Majorana particles and provide a direct measure of neutrino mass. For a recent review, see [91]. The signal in $0\nu\beta\beta$ decay is distinctive: the full Q-value energy of the nuclear decay appears as equal energy back-to-back recoil electrons. A large TPC is advantageous for observing this low rate decay for all the reasons described above. The first detector to observe the standard model process 2 neutrino double beta decay was a gaseous TPC which imaged the two electrons tracks from ^{82}Se embedded in a foil. Modern detectors use Xe as the detector medium because it includes the $\beta\beta$ isotope ^{136}Xe (Q-value 2458 keV), which, as an inert gas, can also be more readily enriched from its natural 8.9% abundance than any other $\beta\beta$ isotope. EXO-200, which currently has one of the best search limits [93], is a large single-phase LXe TPC with roughly 110 active kg of Xe enriched to 80.7 % ^{136}Xe, and a multi-ton successor nEXO has been proposed which would fully cover the inverted neutrino mass hierarchy. These detectors are similar to dark matter TPCs, but, not needing charge gain, use single phase with charge measured directly on crossed wire grids. Light readout is done with LAAPDs

(EXO-200) and SiPMTs (nEXO).

The dominant background is gamma rays originating outside the active volume. Most of these undergo multiple Compton-scatters which are efficiently recognized and rejected through sub-cm position resolution, though the few percent of gammas at this energy that photoabsorb are not. Self shielding of gamma rays is less powerful than in dark matter, since in the former case there is some small probability of penetrating to some depth followed by the modestly small probability of photo-absorption. The latter case consists of three small probability processes: penetration to some depth, a very low-energy scatter, and the gamma exiting without a second interaction. Because of this and the fact that background and the signal are both electron recoils, the requirements on radioactivity in all the materials of a $\beta\beta$ TPC are much more stringent than an otherwise similar dark matter detector, unless other background rejection tools are available. Percent-level energy resolution is crucial to avoid background from $2\nu\beta\beta$ decays and gammas including the prominent 2615 MeV line from ^{208}Tl in the Th chain. Here the combined charge and light measurement eliminates the otherwise dominant fluctuations in recombination which lead to anti-correlated fluctuations in charge and light. EXO-200 has achieved $\sigma \approx$ 1.5% (at 2458 keV), and values below 1% appear possible.

A related approach being pursued by the NEXT and PandaX-III collaborations is to use high pressure gaseous Xe TPC. With mm-scale charge readout, the two-electron topology of $0\nu\beta\beta$ events can be distinguished from single electrons from photoabsorption of background gammas. In addition, the low recombination fraction in the gas phase suppresses recombination fluctuations, in principle allowing σ below 0.2% via the charge channel alone. Finally, a definitive identification of a $0\nu\beta\beta$ signal would be provided by extraction and tagging of the ionized Ba daughter via atomic physics techniques [94], either in gas or liquid and gas phases.

35.5. Sub-Kelvin detectors

Written September 2015 by K. Irwin (Stanford and SLAC).

Many particle physics experiments utilize detectors operated at temperatures below 1 K. These include WIMP searches, beta-decay experiments to measure the absolute mass of the electron neutrino, and searches for neutrinoless-double-beta decay ($0\nu\beta\beta$) to probe the properties of Majorana neutrinos. Sub-Kelvin detectors also provide important cosmological constraints on particle physics through sensitive measurement of the cosmic microwave background (CMB). CMB measurements probe the physics of inflation at $\sim 10^{16}$ GeV, and the absolute mass, hierarchy, and number of neutrino species.

Detectors that operate below 1 K benefit from reduced thermal noise and lower material specific heat and thermal conductivity. At these temperatures, superconducting materials, sensors with high responsivity, and cryogenic preamplifiers and multiplexers are available. We provide a simple overview of the techniques and the experiments using sub-K detectors. A useful review of the broad application of low-temperature detectors is provided in [95], and the proceedings of the International Workshop on Low Temperature Detectors [96] provide an overview of the field.

Sub-Kelvin detectors can be categorized as equilibrium thermal detectors or non-equilibrium detectors. Equilibrium detectors measure a temperature rise in a material when energy is deposited. Non-equilibrium detectors are based on the measurement of prompt, non-equilibrated signals and on the excitation of materials with an energy gap.

35.5.1. *Equilibrium thermal detectors* :

An equilibrium thermal detector consists of a thermometer and absorber with combined heat capacity C coupled to a heat bath through a weak thermal conductance G. The rise time of a thermal detector is limited by the internal equilibration time of the thermometer-absorber system and the electrical time constant of the thermometer. The thermal relaxation time over which heat escapes to the heat bath is $\tau = C/G$. Thermal detectors are often designed so that an energy input to the absorber is thermalized and equilibrated through the absorber and thermometer on timescales shorter than τ, making the operation particularly simple. An equilibrium thermal detector can be operated as either a calorimeter, which measures an incident energy deposition E, or as a bolometer, which measures an incident power P.

In a calorimeter, an energy E deposited by a particle interaction causes a transient change in the temperature $\Delta T = E/C$, where the heat capacity C can be dominated by the phonons in a lattice, the quasiparticle excitations in a superconductor, or the electronic heat capacity of a metal. The thermodynamic energy fluctuations in the absorber and thermometer have variance

$$\Delta E^2_{\mathrm{rms}} = k_{\mathrm{B}} T^2 C \tag{35.5}$$

when operated near equilibrium, where ΔE_{rms} is the root-mean-square energy fluctuation, k_{B} is the Boltzmann constant and T is the equilibrium temperature. When a sufficiently sensitive thermometer is used, and the energy is thermalized at frequencies large compared to the thermal response frequency ($f_{\mathrm{th}} = 1/2\pi\tau$), the signal-to-noise ratio is nonzero at frequencies higher than f_{th}. In this case, detector energy resolution can be somewhat better than ΔE_{rms} [97]. Deviations from the ideal calorimeter model can cause excess noise and position and energy dependence in the signal shape, leading to degradation in achieved energy resolution.

In a bolometer, a power P deposited by a stream of particles causes a change in the equilibrium temperature $\Delta T = P/G$. The weak thermal conductance G to the heat bath is usually limited by the flow of heat through a phonon or electron system. The thermodynamic power fluctuations in the absorber and thermometer have power spectral density

$$S_{\mathrm{P}} = NEP^2 = 4 k_{\mathrm{B}} T^2 G \tag{35.6}$$

when operated near equilibrium, where the units of NEP (noise equivalent power) are $\mathrm{W}/\sqrt{\mathrm{Hz}}$.

The minimization of thermodynamic energy and power fluctuations is a primary motivation for the use of sub-Kelvin thermal detectors. These low temperatures also enable the use of materials and structures with extremely low C and G, and the use of superconducting materials and amplifiers.

When very large absorbers are required (e.g. WIMP dark matter searches), dielectric crystals with extremely low specific heat are often used. These materials are operated well below the Debye temperature T_{D} of a crystal, where the specific heat scales as T^3. In this low-temperature limit, the dimensionless phononic heat capacity at fixed volume reduces to

$$\frac{C_{\rm V}}{N\,k_{\rm B}} = \frac{12\,\pi^4}{5}\left(\frac{T}{T_{\rm D}}\right)^3 , \tag{35.7}$$

where N is the number of atoms in the crystal. Normal metals have higher low-temperature specific heat than dielectric crystals, but they also have superior thermalization properties, making them attractive for some applications in which extreme precision and high energy resolution are required (e.g. beta endpoint experiments to measure neutrino mass using ^{163}Ho). At low temperature, the heat capacity of normal metals is dominated by electrons, and is linear in temperature, with convenient form

$$C = \frac{\rho}{A}\gamma V T, \tag{35.8}$$

where V is the sample volume, γ is the molar specific heat of the material, ρ is the mass density, and A is the atomic weight. Superconducting absorbers are also used. Superconductors combine some of the thermalization advantages of normal metals with the lower specific heats associated with insulators when operated well below $T_{\rm c}$, where the electronic heat capacity freezes out, and the material is dominated by phononic heat capacity. At higher temperatures, superconducting materials have more complicated heat capacities, but at their transition temperature $T_{\rm c}$, BCS theory predicts that the electronic heat capacity of a superconductor is ∼2.43 times the normal metal value.

When very low thermal conductances are required for power measurement (e.g. the measurement of the cosmic microwave background), the weak thermal link is sometimes provided by thin membranes of non-stoichiometric silicon nitride. The thermal conductance of these membranes is:

$$G = 4\sigma A T^3 \xi, \tag{35.9}$$

where σ has a value of 15.7 mW/cm^{2}K^4, A is the cross-sectional area perpendicular to the heat flow, and ξ is a numerical factor with a value of one in the case of specular surface scattering but less than one for diffuse surface scattering. The thermal impedance between the electron and phonon systems can also limit the thermal conductance.

The most commonly used sub-Kelvin thermometer is the superconducting transition-edge sensor (TES) [98]. The TES consists of a superconductor biased at the transition temperature $T_{\rm c}$, in the region between the superconducting and normal state, where its resistance is a strong function of temperature. The TES is voltage biased. The Joule power provides strong negative electrothermal feedback, which improves linearity, speeds up response to faster than $\tau = C/G$, and provides tolerance for $T_{\rm c}$ variation between multiple TESs in a large array. The current flowing through a TES is read out by a superconducting quantum interference device (SQUID) amplifier. These amplifiers can be cryogenically multiplexed, allowing a large number of TES devices to be read out with a small number of wires to room temperature.

Neutron-transmutation-doped (NTD) germanium and implanted silicon semiconductors read out by cryogenic FET amplifiers are also used as thermometers [97]. Their electrical resistance is exponentially dependent on $1/T$, and is determined by phonon-assisted

Table 35.6: Some selected experiments using sub-Kelvin equilibrium bolometers to measure the CMB. These experiments constrain the physics of inflation and the absolute mass, hierarchy, and number of neutrino species. The experiment location determines the part of the sky that is observed. The size of the aperture determines the angular resolution. The table also indicates the type of sensor used, the number of sensors, the frequency range, and the number of frequency bands. The number of sensors and frequency range and bands for ongoing upgrades are provided for some experiments in parentheses.

Sub-K CMB Experiment	Location	Aperture	Sensor type	# Sensors (planned)	Frequency (planned)	Bands (planned)
Ground-based						
Atacama Cosmology Telescope (2007–)	Chile	6 m	TES	1,800 (5,334)	90–150 GHz (28–220 GHz)	2 (5)
BICEP/Keck (2006–)	South Pole	26/68 cm	TES	3,200	95–220 GHz	3
CLASS (2015–)	Chile	60 cm	TES	36 (5,108)	40 GHz (40–220 GHz)	1 (4)
POLARBEAR / Simons (2012–)	Chile	3.5 m	TES	1,274 (22,764)	150 GHz (90–220 GHz)	1 (3)
South Pole Telescope (2007–)	South Pole	10 m	TES	1,536 (16,260)	95–150 GHz (95–220 GHz)	2 (3)
Balloon						
EBEX (2013–)	McMurdo	1.5 m	TES	∼1,000	150–410 GHz	3
PIPER (2016–)	New Mexico	2 m	TES	5,120	200–600 GHz	4
SPIDER (2014–)	McMurdo	30 cm	TES	1,959	90–280 GHz	3
Satellite						
Planck HFI (2003–)	L2	1.5 m	NTD	52	100-857 GHz	9

hopping conduction between impurity sites. Finally, the temperature dependence of the permeability of a paramagnetic material is used as a thermometer. Detectors using these thermometers are referred to as metallic magnetic calorimeters (MMC) [99]. These detectors operate without dissipation and are inductively readout by SQUIDs.

Equilibrium thermal detectors are simple, and they have important advantages in precision measurements because of their insensitivity to statistical variations in energy down-conversion pathways, as long as the incident energy equilibrates into an equilibrium thermal distribution that can be measured by a thermometer.

35.5.2. *Nonequilibrium Detectors* :

Nonequilibrium detectors use many of the same principles and techniques as equilibrium detectors, but are also sensitive to details of the energy down-conversion before thermalization. Sub-Kelvin nonequilibrium detectors measure athermal phonon signals in a dielectric crystal, electron-hole pairs in a semiconductor crystal, athermal quasiparticle excitations in a superconductor, photon emission from a scintillator, or a combination of two of the above to better discriminate recoils from nuclei or electrons. Because the phonons are athermal, sub-Kelvin nonequilibrium detectors can use absorbers with larger heat capacity, and they use information about the details of energy down-conversion pathways in order to better discriminate signal from background.

In WIMP and neutrino experiments using sub-Kelvin dielectric semiconductors, the recoil energy is typically $\gtrsim 0.1$ keV. The majority of the energy is deposited in phonons and a minority in ionization and, in some cases, scintillation. The semiconductor bandgap is typically $\sim$ eV, and $k_{\rm B}T < 10\ \mu$eV at $T < 1$ K. Thus, high-energy charge pairs and athermal phonons are initially produced. The charge pairs cascade quickly to the gap edge. The high-energy phonons experience isotopic scattering and anharmonic decay, which downshifts the phonon spectrum until the phonon mean free path approaches the characteristic dimension of the absorber. If the crystal is sufficiently pure, these phonons propagate ballistically, preserving information about the interaction location. They are not thermalized, and thus not affected by an increase in the crystal heat capacity, allowing the use of larger absorbers. Sensors similar to those used in sub-K equilibrium thermal detectors measure the athermal phonons at the crystal surface.

Superconductors can also be used as absorbers in sub-Kelvin detectors when $T \ll T_{\rm c}$. The superconducting gap is typically $\sim$ meV. Energy absorption breaks Cooper pairs and produces quasiparticles. These particles cascade to the superconducting gap edge, and then recombine after a material-dependent lifetime. During the quasiparticle lifetime, they diffuse through the material. In superconductors with large mean free path, the diffusion length can be more than 1 mm, allowing diffusion to a detector.

In some experiments (e.g. SuperCDMS and CRESST), athermal phonons and quasiparticle diffusion are combined to increase achievable absorber mass. Athermal phonons in a three-dimensional dielectric crystal break Cooper pairs in a two-dimensional superconducting film on the detector surface. The resulting quasiparticles diffuse to thermal sensors (typically a TES) where they are absorbed and detected. While thin superconducting films have diffusion lengths shorter than the diffusion lengths in single crystal superconductors, segmenting the films into small sections and coupling them to multiple TES sensors allows the instrumentation of large absorber volume. The TES sensors can be wired in parallel to combine their output signal.

The combined measurement of the phonon signal and a secondary signal (ionization or scintillation) can provide a powerful discrimination of signal from background events. Nuclear-recoil events in WIMP searches produce proportionally smaller ionization or scintillation signal than electron-scattering events. Since many of the background events are electron recoils, this discrimination provides a powerful veto. Similarly, beta-decay events produce proportionally smaller scintillation signal than alpha-particle events, allowing rejection of alpha backgrounds in neutrino experiments.

Table 35.7: Selected experiments using sub-Kelvin calorimeters. The table shows only currently operated experiments, and is not exhaustive. WIMP experiments search for dark matter, and beta-decay and neutrinoless double beta decay ($0\nu\beta\beta$) experiments constrain neutrino mass, hierarchy, and Majorana nature. The experiment location determines the characteristics of the radioactive background. The dates of current program phase, detection mode (equilibrium or nonequilibrium phonon measurements, and measurement of ionization or scintillation signals), the absorber and total mass, the sensor type, and the number of sensors and crystals (if different) are given. Many sub-K calorimeter experiments are also in planning and construction phases, including EURECA (dark matter), HOLMES and NuMECs (beta decay), and CUPID-0 ($0\nu\beta\beta$ decay). Many of the existing experiments are being upgraded to larger mass absorbers, different absorber materials, or lower energy threshhold.

Sub-K Calorimeter	Location	Detection mode	Absorber Total mass	Sensor type	# Sensor # Crystal
WIMP					
CRESST II (2003–)	Gran Sasso Italy	Noneq. phon. and scint.	$CaWO_4$ 5.4 kg	TES	18
EDELWEISS III (2015–)	LSM Modane France	Eq. thermal and ion.	Ge 22 kg	NTD Ge +HEMT	36
SuperCDMS (2012–)	Soudan, USA SNOLAB, Canada	Noneq. phon. and ion.	Ge 9 kg	TES +JFET	120 15
Beta decay					
ECHo (2012–)	Heidelberg Germany	Eq. thermal	Au:^{163}Ho 0.2μg	MMC	16
$0\nu\beta\beta$ decay					
CUORE (2015–)	Gran Sasso Italy	Eq. thermal	TeO_2 741 kg	NTD Ge	988
AMoRe Pilot (2015–)	Yang Yang S. Korea	Noneq. phon. and scint.	$CaMoO_4$ 1.5 kg	MMC	5
LUCIFER (2010–)	Gran Sasso Italy	Eq. thermal and scint.	ZnSe 431 g	NTD Ge	1

Combined phonon and ionization measurement has been implemented in experiments including CDMS I/II, SuperCDMS, and EDELWEISS I/II/III. These experiments use semiconductor crystal absorbers, in which dark-matter scattering events would produce recoiling particles and generate electron-hole pairs and phonons. The electron-hole pairs are separated and drifted to the surface of the crystal by applying an electric field, where they are measured by a JFET or HEMT using similar techniques to those used in

77 K Ge x-ray spectrometers. However, the field strength must be much lower in sub-K detectors to limit the generation of phonon signals by the Neganov-Luke effect, which can confuse the background discrimination. For detectors with very low threshhold, the Neganov-Luke effect can also be used to detect generated charge through the induced phonon signal.

Combined phonon and scintillation measurement has been implemented in CRESST II, ROSEBUD, AMoRE and LUCIFER. For example, the CRESST-II experiment uses $CaWO_4$ crystal absorbers, and measures both the phonon signal and the scintillation signal with TES calorimeters. A wide variety of scintillating crystals are under consideration, including different tungstates and molybdates, BaF_2, ZnSe, and bismuth germanate (BGO).

35.6. Low-radioactivity background techniques

Revised August 2015 by A. Piepke (University of Alabama).

The physics reach of low-energy rare-event searches *e.g.* for dark matter, neutrino oscillations, or double beta decay is often limited by background caused by radioactivity. Depending on the chosen detector design, the separation of the physics signal from this unwanted interference can be achieved on an event-by-event basis by active event tagging, utilizing some unique event features, or by reducing the flux of the background radiation by appropriate shielding and material selection. In both cases, the background rate is proportional to the flux of the interfering radiation. Its reduction is thus essential for realizing the full physics potential of the experiment. In this context, “low energy” may be defined as the regime of natural, anthropogenic, or cosmogenic radioactivity, all at energies up to about 10 MeV. See [100,101] for in-depth reviews of this subject. Following the classification of [100], sources of background may be categorized into the following classes:

1. environmental radioactivity,
2. radio-impurities in detector or shielding components,
3. radon and its progeny,
4. cosmic rays,
5. neutrons from natural fission, (α, n) reactions and from cosmic-ray muon spallation and capture.

35.6.1. ***Defining the problem*** : The application defines the requirements. Background goals can be as demanding as a few low-energy events per year in a ton-size detector. The strength of the physics signal of interest can often be estimated theoretically or from limits derived by earlier experiments. The experiments are then designed for the desired signal-to-background ratio. This requires finding the right balance between “clarity of measurement”, ease of construction, and budget. In a practical sense, it is important to formulate background goals that are sufficient for the task at hand but achievable, in a finite time. It is standard practice to use detector simulations to translate the background requirements into limits for the radioactivity content of various detector components, requirements for radiation shielding, and allowable cosmic-ray fluxes. This strategy allows the identification of the most critical components early and facilitates the allocation of analysis and development resources in a rational way. The CERN code GEANT4 [102] is a widely used tool for this purpose. It has incorporated sufficient nuclear physics to allow accurate background estimations. Custom-written event generators, modeling *e.g.*, particle correlations in complex decay schemes, deviations from allowed beta spectra or $\gamma - \gamma$-angular correlations, are used as well.

35.6.2. ***Environmental radioactivity*** : The long-lived natural radio-nuclides ^{40}K, ^{232}Th, and ^{238}U have average abundances of 1.6, 11.1 and 2.7 ppm (corresponding to 412, 45 and 33 Bq/kg, respectively) in the earth's crust, with large local variations. In most applications, γ radiation emitted due to the decay of natural radioactivity and its unstable daughters constitutes the dominant contribution to the local radiation field. Typical low-background applications require levels of natural radioactivity on the order of ppb or ppt in the detector components. Passive or active shielding is used to suppress external γ radiation down to an equivalent level. Fig. 35.10 shows the energy-dependent attenuation length $\lambda(E_\gamma)$ as a function of γ-ray energy E_γ for three common shielding materials (water, copper, lead). The thickness ℓ required to reduce the external flux by a factor $f > 1$ is estimated, assuming exponential damping:

$$\ell \;=\; \lambda(E_\gamma) \cdot \ln f \; . \tag{35.10}$$

At 100 keV, a typical energy scale for dark matter searches (or 2.615 MeV, for a typical double-beta decay experiment), attenuation by a factor $f = 10^5$ requires 67(269) cm of H_2O, 2.8(34) cm of Cu, or 0.18(23) cm of Pb. Such estimates allow for an order-of-magnitude determination of the experiment dimensions.

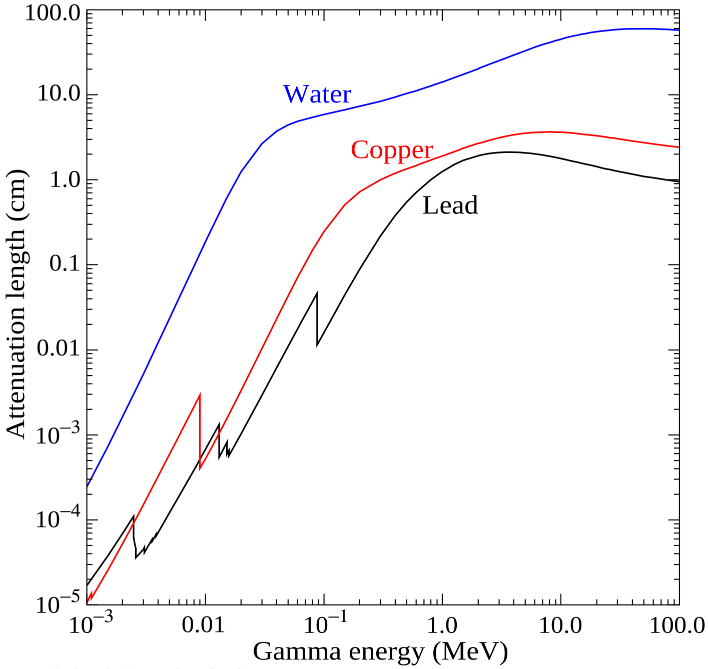

Figure 35.10: γ-ray attenuation lengths in some common shielding materials. The mass attenuation data has been taken from the NIST data base XCOM; see "Atomic Nuclear Properties" at `pdg.lbl.gov`.

A precise estimation of the the magnitude of the external gamma-ray background, including scattering and the effect of analysis-energy cuts, requires Monte Carlo simulations based on the the knowledge of the radioactivity present in the laboratory. Detailed modeling of the γ-ray flux in a large laboratory, or inside the hermetic shielding, needs to cope with a very small probability of generating any signal in the detector. It is often advantageous to calculate solid angle of the detector to the background sources and mass attenuation of the radiation shield separately, or to employ importance sampling. The former method can lead to loss of energy-direction correlations while in the latter has to balance CPU-time consumption against the loss of statistical independence. These approaches reduce the computation time required for a statistically meaningful number of detector hits to manageable levels.

Water is commonly used as shielding medium for large detectors, as it can be obtained cheaply and purified effectively in large quantity. Water purification technology is commercially available. Ultra-pure water, instrumented with photomultiplier tubes, can serve as active cosmic-ray veto counter. Water is also an effective neutron moderator and shield. In more recent underground experiments that involve detectors operating at cryogenic temperature, liquefied gases (e.g. argon) are being used for shielding as well.

35.6.3. ***Radioactive impurities in detector and shielding components*** : After suppressing the effect of external radioactivity, radioactive impurities, contained in the detector components or attached to their surfaces, become important. Every material contains radioactivity at some level. The activity can be natural, cosmogenic, man-made, or a combination of them. The determination of the activity content of a specific material or component requires case-by-case analyses, and is rarely obtainable from the manufacturer. However, there are some general rules that can be used to guide the pre-selection. For detectors designed to look for electrons (for example in double-beta decay searches or neutrino detection via inverse beta decay or elastic scattering), intrinsic radioactivity is often the principal source of background. For devices detecting nuclear recoils (for example in dark matter searches), this is often of secondary importance as ionization signals can be actively discriminated on an event-by-event basis. Decay induced nuclear reactions become a concern.

For natural radioactivity, a rule of thumb is that synthetic substances are cleaner than natural materials. Typically, more highly processed materials have lower activity content than raw substances. Substances with high electro-negativity tend to be cleaner as the refining process preferentially removes K, Th, and U. For example, Al is often found to contain considerable amounts of Th and U, while electrolytic Cu is very low in primordial activities. Plastics or liquid hydrocarbons, having been refined by distillation, are often quite radiopure. Tabulated radioassay results for a wide range of materials can be found in Refs. [103] and [104]. Radioassay results from previous underground physics experiments are being archived at an online database [105].

The long-lived ^{238}U daughter ^{210}Pb ($T_{1/2}$=22.3 y) is found in all shielding lead, and is a background concern at low energies. This is due to the relatively high endpoint energy (Q_β=1.162 MeV) of its beta-unstable daughter ^{210}Bi. Lead refined from selected low-U ores have specific activities of about 5–30 Bq/kg. For applications that require lower specific activity, ancient lead (for example from Roman ships) is sometimes used.

Because the ore processing and lead refining removed most of the ^{238}U, the ^{210}Pb decayed during the long waiting time to the level supported by the U-content of the refined lead. Lining the lead with copper to range out the low-energy radiation is another remedy. However, intermediate-Z materials carry additional cosmogenic-activation risks when handled above ground, as will be discussed below. ^{210}Pb is also found in solders.

Man-made radioactivity, released during above-ground nuclear testing and nuclear power production, is a source of background. The fission product ^{137}Cs can often be found attached to the surface of materials. The radioactive noble gas ^{85}Kr, released into the atmosphere by nuclear reactors and nuclear fuel re-processing, is sometimes a background concern, especially due to its high solubility in organic materials. Post-World War II steel typically contains a few tens of mBq/kg of ^{60}Co.

Surface activity is not a material property per se but is added during manufacturing and handling. Surface contamination can often be effectively removed by clean machining, etching, or a combination of both. The assembly of low-background detectors is often performed in controlled enclosures (e.g. clean rooms or glove boxes) to avoid contaminating surfaces with environmental substances, such as dust, containing radioactivity at much higher concentrations than the detector components. Surfaces are cleaned with high purity chemicals and de-ionized water. When not being processed components are best stored in sealed bags to limit dust deposition on the surface, even inside clean rooms. Surface contamination can be quantified by means of wipe-testing with acid or alcohol wetted Whatman 41 filters. Pre-soaking of the filters in clean acid reduces the amount of Th and U contained in the paper and boosts analysis sensitivity. The paper filters are ashed after wiping and the residue is digested in acid. Subsequent analysis by means of mass spectroscopy or neutron activation analysis is capable of detecting less than 1 pg/cm^2 of Th and U.

The most demanding low-rate experiments require screening of *all* components, which can be a time consuming task. The requirements for activity characterization depend on the experiment and the location and amount of a particular component. Monte Carlo simulations are used to quantify these requirements. Sensitivities of the order μBq/kg or less are sometimes required for the most critical detector components. At such a level of sensitivity, the characterization becomes a challenging problem in itself. Low-background α, β, and γ-ray counting, mass spectroscopy, and neutron activation analysis are the commonly used diagnostic techniques.

35.6.4. ***Radon and its progeny*** : The noble gas ^{222}Rn, a pure α-emitter, is a ^{238}U decay product. Due to its relatively long half-life of 3.8 d it is released by surface soil and is found in the atmosphere everywhere. ^{220}Rn (^{232}Th decay product) is mostly unimportant for most low-background experiments because of its short half-life. The ^{222}Rn activity in air ranges from 10 to 100 mBq/L outdoors and 100 to thousands of mBq/L indoors. The natural radon concentration depends on the weather and shows daily and seasonal variations. Radon levels are lowest above the oceans. For electron detectors, it is not the Rn itself that creates background, but its progeny ^{214}Pb, ^{214}Bi, ^{210}Bi, which emit energetic beta and γ radiation. Thus, not only the detector itself has to be separated from contact with air, but also internal voids in the shield which contain air can be a background concern. Radon is quite soluble in water and even more so in organic solvents. For large liquid scintillation detectors, radon mobility due to convection and diffusion is a concern. To define a scale: typical double-beta-decay searches are are restricted to $< \mu\mathrm{Bq/kg_{detector}}$ (or 1 decay per $\mathrm{kg_{detector}}$ and per 11.6 days) activities of ^{222}Rn in the active medium. This corresponds to a steady-state population of 0.5 atoms/$\mathrm{kg_{detector}}$ or 50 $\mu\mathrm{L/kg_{detector}}$ of air (assuming 20 mBq/L of radon in the air). The demand on leak tightness can thus be quite demanding. The decay of Rn itself is a concern for some recoil type detectors, as nuclear recoil energies in α decays are substantial (76 keV in the case of ^{222}Rn).

Low-background detectors are often kept sealed from the air and continuously flushed with boil-off nitrogen, which contains only small amounts of Rn. For the most demanding applications, the nitrogen is purified by multiple distillations, or by using pressure swing adsorption chromatography. Then only the Rn outgassing of the piping (due to its intrinsic U content) determines the radon concentration. Radon diffuses readily through thin plastic barriers. If the detector is to be isolated from its environment by means of a membrane, the choice of material is important [106].

Prolonged exposure of detector components or raw materials to air leads to the accumulation of the long-lived radon daughter ^{210}Pb on surfaces. Due to its low Q-value of 63.5 keV, ^{210}Pb itself is only a problem when extreme low energy response is important. However, because of its higher Q-value, the lead daughter ^{210}Bi, is a concern up to the MeV scale. The alpha unstable Bi-daughter ^{210}Po ($E_\alpha = 5304$ keV) contributes not only to the alpha background but can also induce the emission of energetic neutrons via (α,n) reactions on low-Z materials (such as F, C, Si...etc). The neutrons, in turn, may capture on other detector components, creating energetic background. The (α,n) reaction yield induced by the α decay of ^{210}Po is typically small ($6 \cdot 10^{-6}$ n/α in Teflon, for example). Some data is available on the deposition of radon daughters from air onto materials, see e.g. [108]. This data indicates effective radon daughter collection distances of a a few *cm* in air. These considerations limit the allowable air exposure time. In case raw materials (e.g. in the form of granules) were exposed to air at the production site, the bulk of the finished detector components may be loaded with ^{210}Pb and its daughters. These are difficult to detect as no energetic gamma radiation is emitted in their decays. Careful air-exposure management is the only way to reduce this source of background. This can be achieved by storing the parts under a protective low-radon cover gas or keeping them sealed from radon.

State-of-the-art detectors can detect radon even at the level of few atoms. Solid state, scintillation, or gas detectors utilize alpha spectroscopy or are exploiting the fast $\beta - \alpha$ decay sequences of ^{214}Bi and ^{214}Po. The efficiency of these devices is sometimes boosted by electrostatic collection of charged radon from a large gas volume into a small detector.

35.6.5. ***Cosmic rays*** : Cosmic radiation, discussed in detail in Chapter 29, is a source of background for just about any non-accelerator experiment. Primary cosmic rays are about 90% protons, 9% alpha particles, and the rest heavier nuclei (Fig. 29.1). They are totally attenuated within the first the first few hg/cm^2 of atmospheric thickness. At sea level secondary particles ($\pi^\pm : p : e^\pm : n : \mu^\pm$) are observed with relative intensities $1 : 13 : 340 : 480 : 1420$ (Ref. 109; also see Fig. 29.4).

All but the muon and the neutron components are readily absorbed by overburden such as building ceilings and passive shielding. Only if there is very little overburden ($\lesssim$10 g/cm^2 or so [100]) do pions and protons need to be considered when estimating the production rate of cosmogenic radioactivity.

Sensitive experiments are thus operated deep underground where essentially only muons can penetrate. As shown in Fig. 29.7, the muon intensity falls off rapidly with depth. Active detection systems, capable of tagging events correlated in time with cosmic-ray activity, are needed, depending on the overburden.

The muonic background is related to low-radioactivity techniques insofar as photo-nuclear interactions with atomic nuclei can produce long-lived radioactivity directly or indirectly via the creation of neutrons. This happens at any overburden, however, at strongly depth dependent rates. Muon bremsstrahlung, created in high-Z shielding materials, contributes to the low energy background too. Active muon detection systems are effective in reducing this background, but only for activities with sufficiently short half-lives, allowing vetoing with reasonable detector dead time.

Cosmogenic activation of detector components at the surface can be an issue for low-background experiments. Proper management of parts and materials above ground during manufacturing and detector assembly minimizes the accumulation of long-lived activity. Cosmogenic activation is most important for intermediate-Z materials such as Cu and Fe. For the most demanding applications, metals are stored and transported under sufficient shielding to stop the hadronic component of the cosmic rays. Parts can be stored underground for long periods before being used. Underground machine shops are sometimes used to limit the duration of exposure at the surface. Some experiments are even electro-forming copper underground.

35.6.6. ***Neutrons*** : Neutrons contribute to the background of low-energy experiments in different ways: directly through nuclear recoil in the detector medium, and indirectly, through the production of radio-nuclides, capture γs and inelastic scattering inside the detector and its components. The indirect mechanisms allow even remote materials to contribute to the background by means of penetrating γ radiation. Neutrons are thus an important source of low-energy background. They are produced in different ways:

1. At the earth's surface the flux of cosmic-ray secondary neutrons is exceeded only by that of muons;
2. Energetic tertiary neutrons are produced by cosmic-ray muons by nuclear spallation in the detector and laboratory walls;
3. In high-Z materials, often used in radiation shields, nuclear capture of negative muons results in the emission of neutrons;
4. Natural radioactivity has a neutron component through spontaneous fission and (α, n)-reactions.

A calculation with the hadronic simulation code FLUKA [107], using the known energy distribution of secondary neutrons at the earth's surface [110], yields a mass attenuation of 1.5 hg/cm^2 in concrete for secondary neutrons. In case energy-dependent neutron-capture cross sections are known, such calculations can be used to obtain the production rate of particular radio-nuclides.

At an overburden of only few meters water equivalent, neutron production by muons becomes the dominant mechanism. Neutron production rates are high in high-Z shielding materials. A high-Z radiation shield, discussed earlier as being effective in reducing background due to external radioactivity, thus acts as a source for cosmogenic tertiary high-energy neutrons. Depending on the overburden and the radioactivity content of the laboratory, there is an optimal shielding thickness. Water shields, although bulky, are an attractive alternative due to their low neutron production yield and self-shielding.

Shields made from plastic or water are commonly used to reduce the neutron flux. The shield is sometimes doped with a substance having a high thermal neutron capture cross section (such as boron) to absorb thermal neutrons more quickly. The hydrogen, contained in these shields, serves as a target for elastic scattering, and is effective in reducing the neutron energy. Neutrons from natural radioactivity have relatively low energies and can be effectively suppressed by a neutron shield. Ideally, such a neutron shield should be inside the lead to be effective for tertiary neutrons. However, this is rarely done as it increases the neutron production target (in form of the passive shield), and the costs increase as the cube of the linear dimensions. An active cosmic-ray veto is an effective solution, correlating a neutron with its parent muon. This solution works best if the veto system is as far away from the detector as feasible (outside the radiation shield) in order to correlate as many background-producing muons with neutrons as possible. The vetoed time after a muon hit needs to be sufficiently long to assure muon bremsstrahlung and neutron-induced backgrounds are sufficiently suppressed. An upper limit to the allowable veto period is given by the veto-induced deadtime, which is related to the muon hit rate on the veto detector. This consideration also constitutes the limiting factor for the physical size of the veto system (besides the cost). The background caused by neutron-induced radioactivity with live-times exceeding the veto time cannot be addressed in this way. Moving the detector deep underground, and thus reducing the muon flux, is the only technique that addresses all sources of cosmogenic the neutron background.

References:

1. R.M. Baltrusaitis *et al.*, Nucl. Instrum. Methods **A20**, 410 (1985).
2. D.J. Bird *et al.*, The Atrophysics Journal 424,491(1994).
3. T. Abu-Zayyad *et al.*, Nucl. Instrum. Methods **A450**, 253 (2000).
4. H. Tokuno *et al.*, Nucl. Instrum. Methods **A676**, 54 (2012).
5. J. Abraham *et al.* [Pierre Auger Collab.], Nucl. Instrum. Methods **A620**, 227 (2010).
6. J. Abraham *et al.* [Pierre Auger Collab.], Eur. Phys. J. Plus **127**, 94 (2012).
7. T. Fujii et al., Astropart. Phys. **74**, 64 (2016).
8. F. Arqueros, J. Hrandel, and B. Keilhauer, Nucl. Instrum. Methods **A597**, 23 (2008).
9. F. Arqueros, J. Hrandel, and B. Keilhauer, Nucl. Instrum. Methods **A597**, 1 (2008).
10. J. Rosado, F. Blanco, and F. Arqueros, Astropart. Phys. **34**, 164 (2010).
11. J. Boyer *et al.*, Nucl. Instrum. Methods **A482**, 457 (2002);
    J.Abraham *et al.* [Pierre Auger Collab.], Nucl. Instrum. Methods **A620**, 227 (2010).
12. M. Ave *et al.* [AIRFLY Collab.], Astropart. Phys. **28**, 41 (2007).
13. J. Rosado, F. Blanci, and F. Arqueros, Astropart. Phys. **55**, 51 (2014).

14. J.T. Brack *et al.*, Astropart. Phys. **20**, 653, (2004).
15. B. Fick *et al.*, JINST **1**, 11003 (2006).
16. J. Abraham *et al.* [Pierre Auger Collab.], Astropart. Phys. **33**, 108 (2010).
17. J. Abraham *et al.* [Pierre Auger Collab.], Astropart. Phys. **34**, 368 (2011).
18. R. Thalman *et al.* Journal of Quantitative Spectroscopy and Radiative Transfer , **147**, 171 (2014), Erratum-ibid. **189**, 281 (2017).
19. M. Unger *et al.*, Nucl. Instrum. Methods **A588**, 433 (2008).
20. T.K. Gaisser and A.M. Hillas, *Proc. 15th Int. Cosmic Ray Conf.* Bulgarska Akademiia na Naukite, Conf. Papers **8**, 353 (1978), (archived at http://adsabs.harvard.edu/abs/1977ICRC....8..353G).
21. J.Abraham *et al.* [Pierre Auger Collab.], Nucl. Instrum. Methods **A789**, 172 (2015).
22. A. Huangs, G. Medina-Tanco and A. Santangelo, Experimental Astronomy **40**, 1 (2015).
23. P.A. Klimov *et al.* Space Science Reviews, Aug. 21 (2017).
24. G. Abedellaoui *et al.* [JEM-EUSO Collab.], Nucl. Instrum. Methods **A866**, 150, (2017).
25. L. Wiencke and A. Olinto for the JEM-EUSO Collaboration, PoS(ICRC2017) 1097 (2017).
26. A. Olinto et al.,PoS(ICRC2017) 542 (2017).
27. J. Holder *et al.*, AIP Conf. Proc. **1085**, 657 (2008).
28. F. Aharonian *et al.*, Astron. & Astrophys. **457**, 899 (2006).
29. J. Albert *et al.*, Astrophys. J. **674**, 1037 (2008).
30. T.C. Weekes *et al.*, Astrophys. J. **342**, 379 (1989).
31. A.M. Hillas *et al.*, Astrophys. J. **503**, 744 (1998).
32. `http://tevcat.uchicago.edu/`.
33. F.A. Aharonian *et al.*, Astrophys. J. **636**, 777 (2006).
34. M. de Naurois and D. Mazin, Comptes Rendus Physique 16,610(2015).
35. M. Lemoine-Goumard, Proc. 34th ICRC (2015).
36. A.M. Hillas, Astropart. Phys. **43**, 19 (2013).
37. B.S. Acharya *et al.*, Astropart. Phys. **43**, 3 (2013).
38. L.A. Bernstein *et al.*, `arXiv:0907.4183` (2009).
39. Y. Ashie *et al.*, Phys. Rev. **D71**, 112005 (2005).
40. S. Kasuga *et al.*, Phys. Lett. **B374**, 238 (1996).
41. M. Shiozawa, Nucl. Instrum. Methods **A433**, 240 (1999).
42. K. Abe *et al.*, Phys. Rev. **D83**, 052010 (2011).
43. J. Beacom and M. Vagins, Phys. Rev. Lett. **93**, 171101 (2004).
44. J. Boger *et al.*, Nucl. Instrum. Methods **A449**, 172 (2000).
45. T.K. Gaisser, F. Halzen, and T. Stanev, Phys. Reports **258**, 173 (1995) and Phys. Reports **271**, 355 (1995).
46. J.G. Learned and K. Mannheim, Ann. Rev. Nucl. and Part. Sci. **50**, 679 (2000).
47. U.F. Katz and C. Spiering, Prog. in Part. Nucl. Phys. **67**, 651 (2012).
48. M.G. Aartsen et al. (IceCube Collab.), J. Phys. G44, 054006 (2017);.
49. S. Adrián-Martínez et al. (KM3NeT Collab.), J. Phys. G43, 084001 (2016);.

50. A. Avronin et al. (Baikal Collab.), Phys. Part. Nucl. **46**, 211 (2015).
51. M.G. Aartsen et al. (IceCube-Gen2 Collab.), *IceCube-Gen2: A vision for the Future of Neutrino Astronomy in Antarctica*, `arXiv:1412.5106v2 [astro-ph.HE]`.
52. S. Adrián-Martínez et al. (KM3NeT Collab.), Eur. Phys. J. C74, 3056 (2014);
    S. Adrián-Martínez et al. (KM3NeT Collab.), Eur. Phys. J. C76, 54 (2016).
53. M.G. Aartsen *et al.* (IceCube Collab.), Phys. Rev. Lett. 113, 101101 (2014).
54. S. Adrián-Martínez *et al.* (ANTARES Collab.), Astrophys. Journ. 786, L5 (2014).
55. M.G. Aartsen *et al.* (IceCube Collab.), Phys. Rev. D 91, 072004, (2015).
56. J. van Santen (for the IceCube Collab.), contribution to ICRC2017.
57. A. Heijboer (for the ANTARES and KM3NeT Collabs.), contribution to ICRC2017.
58. C. Kopper (for the IceCube Collab.), contribution to ICRC2017.
59. K. Griesen, Phys. Rev. Lett. **16**, 748 (1966);
    G.T. Zatsepin and V.A. Kuzmin, JETP Lett. **4**, 78 (1966).
60. R. Abbasi *et al.* [IceCube Collab.], Astropart. Phys. **34**, 382 (2011).
61. S.R. Klein, `arXiv:1012.1407` (2010).
62. G.A. Askaryan, Sov. Phys. JETP **14**, 441 (1962);
    G.A. Askaryan, Sov. Phys. JETP **21**, 658 (1965).
63. J. Alvarez-Muniz *et al.*, Phys. Rev. **D62**, 063001 (2000).
64. D. Saltzberg *et al.*, Phys. Rev. Lett. **86**, 2802 (2001);
    O. Scholten *et al.*, J. Phys. Conf. Ser. **81**, 012004 (2007).
65. P. Allison *et al.* [ARA Collab.], Astropart. Phys. **70**, 62 (2015).
66. J.C. Hanson *et al.* [ARIANNA Collab.], J. Glaciology **61**, 438 (2015).
67. J. Avva *et al.*, J. Glaciology **61**, 1005 (2015)..
68. A. G. Vieregg, K. Bechtol and A. Romero-Wolf, JCAP **1602**, no. 02, 005 (2016).
69. T. Huege, Braz. J. Phys. **44**, 520 (2014).
70. S. Hoover *et al.*, Phys. Rev. Lett. **105**, 151101 (2010).
71. M. Detrixhe *et al.* [ANITA-II Collab.], Phys. Rev. **D83**, 023513 (2011).
72. R.D. Dagkesamanskii and I.M. Zheleznykh, Sov. Phys. JETP Lett. **50**, 233 (1989).
73. J.D. Bray *et al.*, Phys. Rev. **D91**, 063002 (2015).
74. C. W. James *et al.*, EPJ Web Conf. **135**, 04001 (2017).
75. J.A. Dowdeswell and S. Evans, Rept. on Prog. in Phys. **67**, 1821 (2004).
76. S. Barwick, presented at the 35th Intl. Cosmic Ray Conf. (2017).
77. P. Gorham *et al.* [ANITA Collab.], Phys. Rev. Lett. **103**, 051103 (2009). The published limit is corrected in an erratum, P. Gorham *et al.*, `arXiv:1011.5004` (2010).
78. I. Kravchenko *et al.* [RICE Collab.], Phys. Rev. **D73**, 082002 (2006);
    I. Kravchenko *et al.* [RICE Collab.] Astropart. Phys. **19**, 15 (2003).
79. P. Allison *et al.* [ARA Collab.], Phys. Rev. **D93**, 082003 (2016).
80. S.W. Barwick *et al.* [ARIANNA Collab.], IEEE Trans. Nucl. Sci. **62**, 2202 (2015);
    S.W. Barwick *et al.* [ARIANNA Collab.], Astropart. Phys. **70**, 12 (2015).
81. E. Aprile and T. Doke, Rev. Mod. Phys. **82**, 2053 (2010).
82. V. Chepel and H. Araújo, J. Instrum. **8**, R04001 (2013).
83. T.M. Undagoitia and L. Rauch, `arXiv:1509.08767` (2015).

84. E. Aprile *et al.*, `arXiv:1705.06655` (2017).
85. X. Cui *et al.*, `arXiv:1708.06917` (2017).
86. C.E. Dahl, PhD thesis, Princeton U. (2009).
87. M. Schumann *et al.*, JCAP **10**, 16 (2015).
88. W. Guo and D.N. McKinsey, Phys. Rev. **D87**, 115001 (2013).
89. D.R. Nygren, J. Phys. Conf. Ser. **460**, 012006 (2013).
90. C.A.J. O'Hare *et al.*, Phys. Rev. **D92**, 063518 (2015).
91. S.M. Bilenky and Carlo Giunti, Mod. Phys. Lett. **A27**, 1230015 (2012).
92. J.B. Albert *et al.*, Nature **510**, 229 (2014).
93. J.B. Albert *et al.*, `arXiv:1707.08707` (2017).
94. M.L. Moe, Phys. Rev. **C44**, 931 (1991).
95. C. Enss (ed.), *Cryogenic Particle Detection*, Springer-Verlag, Berlin (2005).
96. E. Shirokoff (ed.), *Proc. 15th Int. Workshop on Low Temperature Detectors (LTD-15)*, J. Low Temp. Phys. **176**, 131–1108 (2014); see also previous *Proceedings* of this workshop.
97. S.H. Moseley, J.C. Mather, and D. McCammon, J. Appl. Phys. **56**, 1257 (1984).
98. K.D. Irwin, Appl. Phys. Lett. **66**, 1998 (1995).
99. S.R. Bandler *et al.*, J. Low. Temp. Phys. **93**, 709 (1993).
100. G. Heusser, Ann. Rev. Nucl. and Part. Sci. **45**, 543 (1995).
101. J.A. Formaggio and C.J. Martoff, Ann. Rev. Nucl. and Part. Sci. **54**, 361 (2004).
102. S. Agostinelli *et al.*, Nucl. Instrum. Methods **A506**, 250 (2003).
103. P. Jagam and J.J. Simpson, Nucl. Instrum. Methods **A324**, 389 (1993).
104. D.S. Leonard *et al.*, Nucl. Instrum. Methods **A591**, 490 (2008).
105. `http://www.radiopurity.org`.
106. M. Wojcik *et al.*, Nucl. Instrum. Methods **A449**, 158 (2000).
107. `http://www.fluka.org/fluka.php?id=faq&sub=13`.
108. V.E. Guiseppe *et al.*, `arXiv:1101.0126` (2011).
109. National Council on Radiation Protection and Measurement, Report 94, Bethesda, MD (1987).
110. M.S. Gordon *et al.*, IEEE Trans. **NS51**, 3427 (2004).